Cross sections and analysing power energy-sharing distributions of valence (p,2p)-knockout from ^{208}Pb with a projectile of 200 MeV

Jacques Bezuidenhout

Thesis submitted in partial fulfilment
of the requirements for the degree of Master of Science
at the University of Stellenbosch

December 2000

Supervisor: Prof A.A. Cowley
Co-supervisor: Dr G.J. Arendse

***Declaration**:*

I, the undersigned, hereby declare that the work in this thesis is my own original work and that I have not previously in its entirety or part submitted it at any university for a degree.

CROSS SECTIONS AND ANALYSING POWER ENERGY-SHARING DISTRIBUTIONS OF VALENCE (p,2p)-KNOCKOUT FROM ^{208}Pb WITH A PROJECTILE OF 200 MeV

Jacques Bezuidenhout

University of Stellenbosch

December 2000

ABSTRACT

The aim of this work was to study the ^{208}Pb(p,2p)^{207}Tl quasi-free knockout process. The experimental data were measured at the National Accelerator Centre using incident polarised protons of 200 MeV. The two scattered particles, from the knockout reaction, were detected in coincidence and their energies were determined using a magnetic spectrometer and a solid state detector telescope.

Cross section and analysing power energy distributions were extracted from the experimental measurements and these were compared with theoretical values for the Distorted Wave Impulse Approximation. The theoretical cross-section calculations predict the experimental cross-section distribution well for all combinations of distorting potentials and bound states that were investigated, both with regard to shape, as well as absolute magnitude. However the theoretical analysing power distributions did not agree with the experimental quantities. Therefore it is not clear whether the analysing power is a useful tool to extract information on the specifics of the quasi-free reaction mechanism. The spectroscopic factors were found to be consistent with the results obtained in previous studies, thereby inspiring confidence that the problem with the analysing power distribution is not ascribable to a possible deficiency in the experimental techniques exploited in this work.

KANSVLAK- EN ANALISEERVERMOË-ENERGIEVERDELINGS VAN VALENS (p,2p)-UITSLAAN UIT ^{208}Pb MET 'N 200 MeV PROJEKTIEL.

Jacques Bezuidenhout

Universiteit van Stellenbosch

Desember 2000

ABSTRAK

Die doel van die studie was om die kwasivrye ^{208}Pb(p,2p)^{207}Tl verstrooingsproses te ondersoek. Die eksperimentele data is ingewin by die Nasionale Versnellingsentrum deur gebruik te maak van 'n 200 MeV gepolariseerde proton bundel. Die twee verstrooide deeltjies is in koïnsidens gemeet. Vir die metings is 'n magnetiese spektrometer en 'n vastetoestand detektorteleskoop gebruik.

Die kansvlak- en analiseervermoë-energieverdelings is uit die eksperimentele data verkry en is vergelyk met die berekenings van die Vervormde Golf Impuls Benadering. Die teoretiese kansvlak berekening het die eksperimetele data goed voorspel, vir die verskillende parametrisering van potensiaal en gebonde toestande. Die berekeninge het goed ooreengestem met betrekking tot beide vorm en absolute grootheid. Die berekende analiseervermoë het egter nie goed met die eksperimentele data ooreengestem nie. Dit is dus nie duidelik of die analiseervermoë 'n handige instrument is om inligting oor die betrokke kwasi-vrye reaksie meganisme te bekom nie. Die spektroskopiese faktore was in ooreenstemming met resultate wat in vorige studies verkry is. Dit versterk vertroue dat die probleem met die analiseervermoë nie toegeskryf kan word aan die eksperimentele tegniek wat gebruik is nie.

ACKNOWLEDGEMENTS

My sincere gratitude goes towards the following people and institutions that contributed towards the success of this study:

-My supervisor Professor A.A. Cowley for all the time he spent to assist me and the outstanding way in which he guided me during this study.

-My co-supervisor Doctor G.J. Arendse for the open door that I always found for questions.

-Mnr R. Neveling for his assistance and advice, especially for aiding me in processing data from Saldanha via the Internet.

-The staff of the National Accelerator Centre for their enormous contribution in conducting the experiment.

-My fellow students and the staff of the University of Stellenbosch who also contributed a great deal towards the final product.

-The staff of the Military Academy for their logistic support, specifically my colleagues for allowing me the time to complete this study.

-Last, but surely not least, I am sincerely thankful to my wife for her support and understanding during this study.

I Korintiërs 13:12

"Nou kyk ons nog in 'n dowwe spieël en sien 'n raaiselagtige beeld, maar eendag sal ons alles sien soos dit werklik is. Nou ken ek net gedeeltelik, maar eendag sal ek ten volle ken soos God my ten volle ken."

TABLE OF CONTENT

Chapter 1: INTRODUCTION

1.1 Overview

This thesis is concerned with a proton knockout reaction from lead, with the ultimate aim to determine whether a theory known as the Distorted Wave Impulse Approximation can successfully reproduce experimentally observed cross section and analysing power distributions. Specifically, the ^{208}Pb(p,2p)^{207}Tl quasi-free scattering process reaction was investigated with a polarised proton beam.

The experimental procedure utilised a magnetic spectrometer in coincidence with a silicon/germanium detector telescope, by means of which the two protons were observed. The material describing the study is organised in the following format: The second section in chapter 1 gives a historical overview. This is followed by a brief description of knockout reactions as pertaining to the field of nuclear physics. The shell model and the optical potential, both related to the structure of the nucleus itself are also discussed. Special reference is made to the so-called quasi-free scattering knockout reaction. The last sections summarise previous work that was done and the objective of this study.

In the second chapter the experimental set-up and procedure that was followed to execute the experiment are explained and the accelerator facility is described. In chapter 3 all the procedures that were followed to achieve data reductions and energy calibrations are discussed. Chapter 4 describes the theoretical models that underlie the interpretation of the results of the experiment. The final results are presented and discussed in chapter 5. In the last chapter, chapter 6, a summary and conclusion are given.

1.2 Historical Overview

Henri Becquerel made the first discovery in the field of nuclear physics when he discovered radioactivity in 1896. Somewhat later in 1911, Rutherford formulated the nuclear atom model, which postulates that the atom contains a nucleus with positive charge, Ze, and almost all the mass of the atom and a negatively charged cloud of particles around the nucleus. The experiment, by means of which this was discovered, used alpha particles emitted by a radium

source. This was of course the very first experimental investigation of a nuclear reaction. Subsequently, by using an accelerated beam of projectiles Chadwick discovered the neutron in 1932, with the result that Heisenberg formulated the proton–neutron nuclear model in the same year. Mayer, Jensen, Haxel and Suess afterwards developed the shell model of nuclear structure in 1949, which proved to be a most successful microscopic model of the atomic nucleus [Wag90].

Clearly one of the most powerful methods to probe the nucleus is through acceleration and collision of particles. Crockcroft and Walton commissioned the first accelerator in 1932 and in the same year Lawrence built the first cyclotron which could deliver particles of higher kinetic energy. By the end of the nineteen forties the first proton synchrocyclotron, accelerating protons up to 350 MeV, was developed at Berkeley. With this accelerator a so-called quasi-free scattering processes could be demonstrated for the first time in 1952 [Jac66]. Thus all the basic theoretical and experimental tools were developed properly and the stage was set to test the shell model of nuclear structure.

1.2 The Shell Model and Knock-out Reactions

The shell model assumes a central potential well, based on the so-called mean field approximation, in which the individual nucleons move. Solving the Schrödinger equation for this potential it follows that the nucleons can only occupy sets of discrete energy levels described by four quantum numbers, i e., the principle quantum number (n), the orbital quantum number (l), the total angular momentum quantum number (j), and the projection of the total angular momentum (m_j). The nucleons in the nucleus are fermions and therefore need to obey the Pauli exclusion principle. This dictates that there cannot be two nucleons with the same set of quantum numbers in the same energy state. The number of nucleons of a specific type, protons or neutrons, which can occupy an orbital, is $2j+1$.

The validity of the shell model may be tested by means of either a knockout or a pick-up reaction. Although the pick-up reactions can be performed with good energy resolution, the incident energy at which this is practicable is rather low, so that those studies are confined to the states near the Fermi surface [Hod71]. The knockout reaction on the other hand can be used to explore the deeper lying states [Jac66]. The knockout reactions can also easily be

used to investigate the binding and separation energies that correspond to the various shells [For92]. Further valuable information on nuclear structure can be obtained by knockout reactions where there are three particles in the final stage [Hod71]. There is a direct relationship between the energies of the reaction products of the (p,2p) reaction and the energies of single–particle state from which the proton was removed. The momentum distributions of the particles in those states can also be determined [Hod71]. In order to study the inner shells by means of knock-out reactions, incoming particles with wavelength comparable with the internucleon separation need to be used. Clearly the wavelength of the particles is only comparable with the internucleon separation in the nucleus, when the energy of the particles is relatively high [Jac66].

The quasi-free scattering process refers to a mechanism in which a projectile knocks a nucleon out of a nucleus, without any further violent interactions occurring between the projectile and the residual nucleus [Jac66]. For such an interaction, incoming protons of moderate (100 MeV-1000 MeV) to high energies (greater than 1000 MeV) are needed. A crude theoretical formulation of the quasi-free scattering process can be developed if two simplifying assumptions are made. The first is that the collision time is short, meaning that the collision can be described by an impulse approximation. The second assumption is that there is no interaction between the incident particle and the target nucleus before the collision and that there is also no interaction between the outgoing particles and the residual nucleus after the collision or between the outgoing particles amongst themselves. These assumptions give rise to the Plane Wave Impulse Approximation (PWIA) treatment. The Distorted Wave Impulse Approximation (DWIA) follows when the second assumption is modified to be more realistic. Both of these approximations are discussed in chapter 4, as the comparison between the primitive and more refined theories provides insight into the physics involved.

1.3 Previous Studies of ^{208}Pb(p,2p)^{207}Tl

Arendse [Are97] performed a study in which he investigated the sensitivity of the DWIA to different selections of the distorting optical potential, making use of the ^{208}Pb(p,2p)^{207}Tl reaction to achieve this. In his work he found that the theory described the data quite well despite the severe distortions due to the heavy target. The different energy states from which protons could be knocked out were not resolved. Thus his investigation did not provide

details of the reaction mechanism as would be possible in a high resolution study of the reaction which could resolve the four lowest energy states of ^{207}Tl (e.g. $3s_{1/2}$, $2d_{3/2}$, $1h_{11/2}$, $2d_{5/2}$). Furthermore, in his study he obtained only cross-sections and spectroscopic factors for this reaction at different angle pairs.

Recently Neveling [Nev98] did a feasibility study to determine if a magnetic spectrometer could be used in coincidence with a ΔE-E detector telescope, (consisting of two elements: one that a particle penetrates with a loss of energy ΔE, followed by one in which the particle deposits the remaining energy E) in order to resolve the four lowest energy states of ^{207}Tl. In order to simplify the initial technical set-up, Neveling chose a NaI(Tl) stopping detector with inferior resolution above a germanium detector. He concluded that the use of the magnetic spectrometer in coincidence with a ΔE-E detector telescope was feasible, and that the NaI(Tl) detector should be replaced by a germanium detector for a proper high-resolution experiment.

1.4 Aim of this Study

In this study the analysing power as well as the cross-section are determined with the prospect of obtaining a resolution comparable to the separation between the lowest energy states of ^{207}Tl. The expectation that the analysing power will be a more sensitive test to compare the predictions of the theory with the experimental data is also tested. The same experimental configuration as Neveling was used, but a germanium detector replaced the NaI(Tl) detector, as was suggested in the feasibility study. This study, furthermore, aims to compare the consistency of the conclusions with those of the earlier work of Arendse [Are97]. A favourable comparison will serve to verify the integrity of the new cross section data, and by implication confirm the quality of the analysing power data.

Chapter 2: THE EXPERIMENT

2.1 Overview

In this chapter the experimental set-up and procedure are discussed. Projectiles from a proton beam were directed at a ^{208}Pb target. In the nuclear reaction that is induced, the incoming proton knocks out another proton from a shell-model orbital of the lead nucleus. The result is two outgoing protons. These two outgoing particles were detected in coincidence and their energy was measured using a K600 magnetic spectrometer and an ΔE-E silicon/germanium detector telescope.

The layout of this chapter is as follows: In the second section some information on the accelerator facility is given. The next two sections discuss the scattering chamber and the proton beam. Sections 2.5 through to 2.8 discuss the detectors that were used during the experiment. In section 2.9 an overview is given of all the electronics required for signal processing. Section 2.10 explains the computer hardware and software responsible for the handling of data, and finally the experimental procedure is described in section 2.11.

2.2 Facility

The experiment was performed at the National Accelerator Centre (NAC) at Faure in the Western Cape. NAC is a multidisciplinary facility providing in the needs of three user communities, being basic nuclear physics research, radiotherapy and a radio-isotope production service. A layout of NAC is shown in *figure 2.1*. The particle beam at NAC is alternated between the different users. During the week radiotherapy and a radio-isotope production share the use (see *figure 2.1* beam line I and vaults TL and TC). The facility is available for fundamental research during weekends. Thus the current experiment was conducted during weekends which covered a period of four weeks.

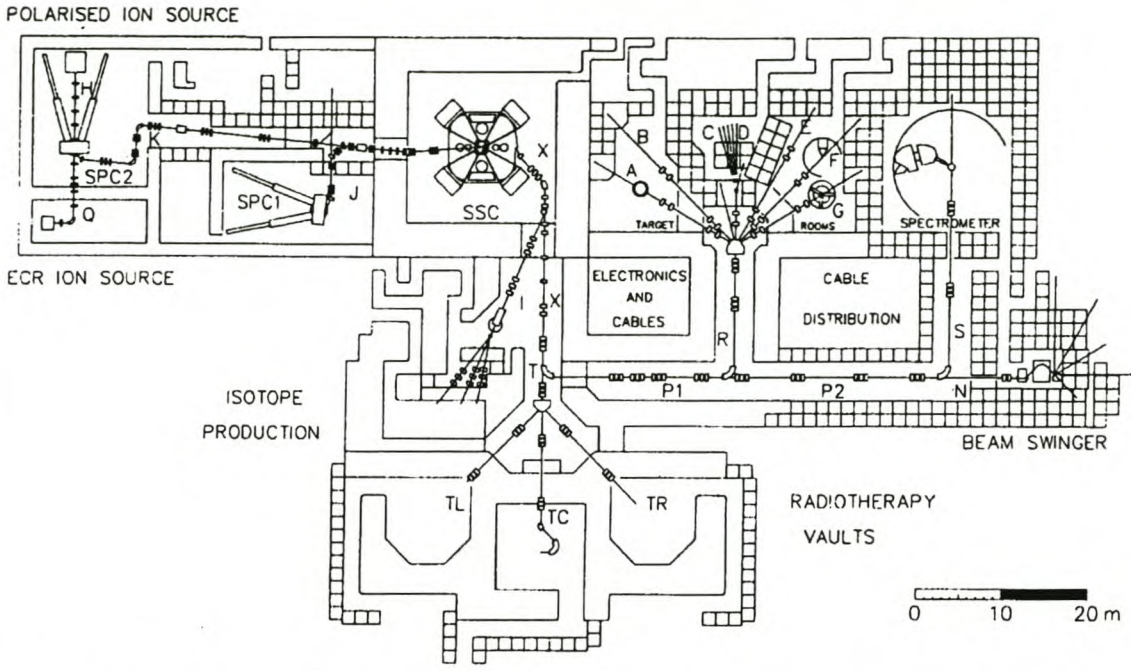

Figure 2.1: Layout of the cyclotron facility of the National Accelerator Centre.

2.3 Proton Beam

A beam of polarised protons was used to bombard an isotopically enriched (98.8%) 7.7 mg/cm^2 thick ^{208}Pb target. Polarised protons were obtained from an ion source, fed by Hydrogen gas. The protons were accelerated to 8 MeV in the second Solid Pole Injector (SPC2). The polarised beam was then transported along beam lines and injected into the Separated Sector Cyclotron (SSC), where the beam energy was increased to 200 MeV.

From the SSC the polarised beam was transported via the high-energy beam lines and delivered to the scattering chamber in the spectrometer vault. Quadrupole magnets were used to focus the polarised beam, while dipole magnets direct the beam to the scattering chamber. The polarised beam then impinged on the lead target positioned in the centre of a scattering chamber.

2.4 Scattering Chamber

The scattering chamber has several ports. These ports are used as feed-throughs for cables and the entrance and exiting beams. One of the ports was used as a window through which a closed circuit video camera views the target position. The whole chamber and the beam line are kept at a vacuum of $\cong 10^{-5}$ mbar. The layout of the scattering chamber in relation to the detectors is shown in *figure 2.2*.

The target ladder has six slots in which the targets were fitted. Target selection was done remotely by moving the target ladder up and down, to select any one of the targets, as needed. The targets used during this experiment were Au, C, $(CH_2)_n$(0.5 gm/cm^2), ^{208}Pb(7.7 mg/cm^2), ruby and an empty position. The first two targets were used for the calculation of the beam offset and the calibration of the detectors.

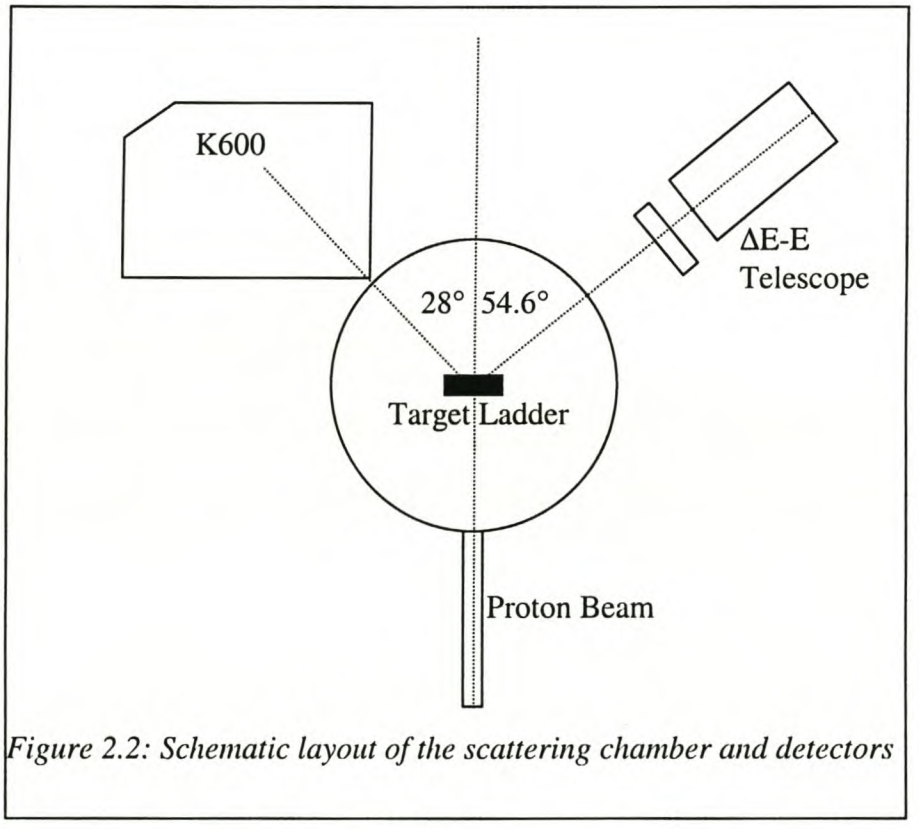

Figure 2.2: Schematic layout of the scattering chamber and detectors

The empty-frame position in the target ladder was used to check the beam halo. The halo indicates the definition of the focused beam on the object. A high-count rate on the empty target indicates that the beam is not focussed properly on the target. Centring the beam spot on the ruby target then aligns the beam. Visible light is produced if the beam collides with

the ruby target. This light is observed with the closed circuit television from the data room, and based on this observed spot, the beam magnets are then adjusted.

The details of the experiment that is performed, determine the angles at which the detectors are placed in relation to the scattering chamber. For this experiment, quasi-free scattering was examined. From the law of conservation of momentum, the angles of the two scattered protons need to add to an angle that is of the order of 90°. But some energy is needed to free the protons from the nucleus, the so-called binding energy (Q). Thus for the conservation of energy, the energy of the incoming proton needs to be equal to the sum of the energies of the outgoing protons plus the binding energy. The angular separation of the outgoing protons is thus less than 90°, which would be the value for free p-p scattering if relativistic effects are neglected.

In this experiment a silicon/germanium (ΔE-E detector telescope) and a K600 spectrometer were used to measure the energies of the outgoing protons. The experiment requires that the outgoing protons deposit all their energy in the detector systems. The germanium detector (15 mm thick) stops protons of a maximum energy of 78 MeV, as calculated with the computer program ELOSS. These relatively low energies for a quasi-free interaction can only be found at angles greater than 47°. The initial angle was thus chosen at 54.6° to coincide with those used by Arendse [Are97]. The angle of the K600 spectrometer was adjusted to an angle slightly smaller than the true quasifree value in order to reduce elastic p-p events, which result from contamination by Hydrogen. The K600 angle was adjusted to be 28° on the opposite side of the beam from the ΔE-E system. The angle of θ_{K600} = 28° and $\theta_{\Delta E\text{-}E}$ = -54.6° are referred to as a quasi-free angle pair because zero recoil momentum is kinematically allowed at those values.

2.5 K600 Spectrometer

This light ion spectrometer is based on the design of the K600 spectrometer at the Indiana University Cyclotron Facility [New96]. The average flight path for a particle from target to detector is approximately 8 m. It is optimised to detect light charged particles, varying from

protons to alpha particles, with good resolution. For protons of 200 MeV, which is the maximum energy from the cyclotron, the best resolution obtained thus far is 27 keV [Nac99].

The K600 spectrometer system consists of a hexapole trim coil, a quadrupole trim coil, a quadrupole and two dipole magnets (*see figure 2.4*). The quadrupole magnet is used for vertical focussing of the beam. The two dipole magnets are the main dispersion elements of the detector [Nev98]. After the particle emerges from the scattering chamber it passes through a collimator to select the particles in the angular acceptance of the magnetic spectrometer.

A selection of particles within a specific momentum range can be obtained by changing the currents in the coils and magnets. A FORTRAN program, SPEXCIT, is used to calculate these currents. The calculations in the program are based upon simple parameterisation modelling of the two-dimensional median plane field maps of the spectrometer magnets.

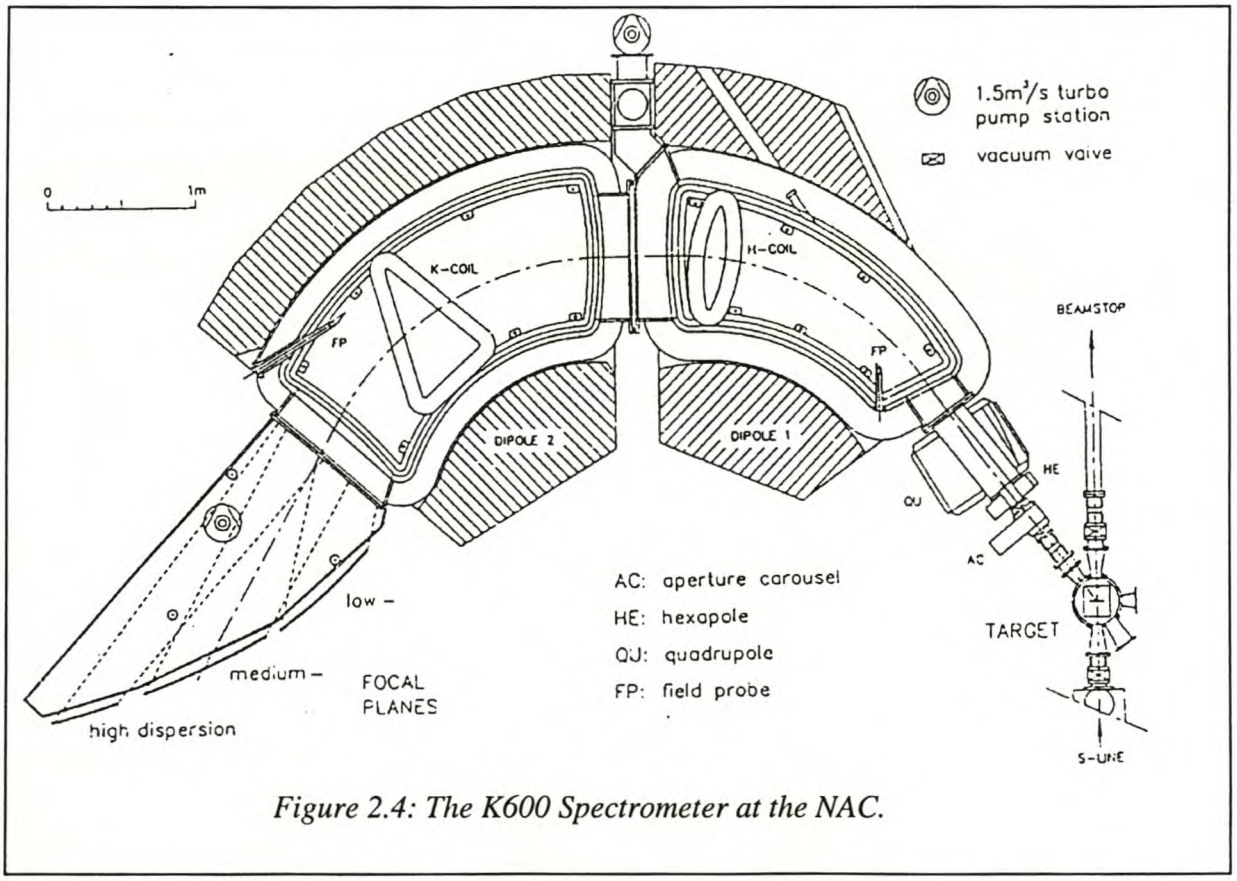

Figure 2.4: The K600 Spectrometer at the NAC.

2.6 Vertical Drift Chamber

The position sensitive detector in the focal plane of the spectrometer, is a vertical drift chamber (VDC). The VDC consists of two high voltage cathode planes and earthed anode signal wires. There are 198 signal wires, 25 μm thick, spaced 4 mm from one another. The signal wires are kept at zero potential. Between each two signal wires there is a guard wire and which is kept at -550 V. The guard wires are 50 μm thick and are made from gold plated tungsten. The signal and guard wires are aligned between the two aluminium foils, serving as cathode planes, and kept at -3.5 kV. Two 25 μm thick Mylar windows are used to seal off the gas-filled interior. (See *figure 2.4)* This gas consists of 90% Ar and 10% CO_2 mixture at atmospheric pressure [New96].

The VDC is placed close to the Kapton exit window of the spectrometer. The wire plane is aligned with the focal plane of the spectrometer. If a particle enters the VDC, some of the gas molecules are ionised. The electrons drift in the electric field, towards the signal wires. Close to the guard wires, Townsend avalanches will be initiated and this will result in a signal on some of the signal wires. If the drift velocity of the electron in the gas is known, the position where the particle crossed the focal plane can be calculated. This is achieved by using the combination of signal wires that fired, in conjunction with the two scintillation detectors (paddles) placed behind the VDC.

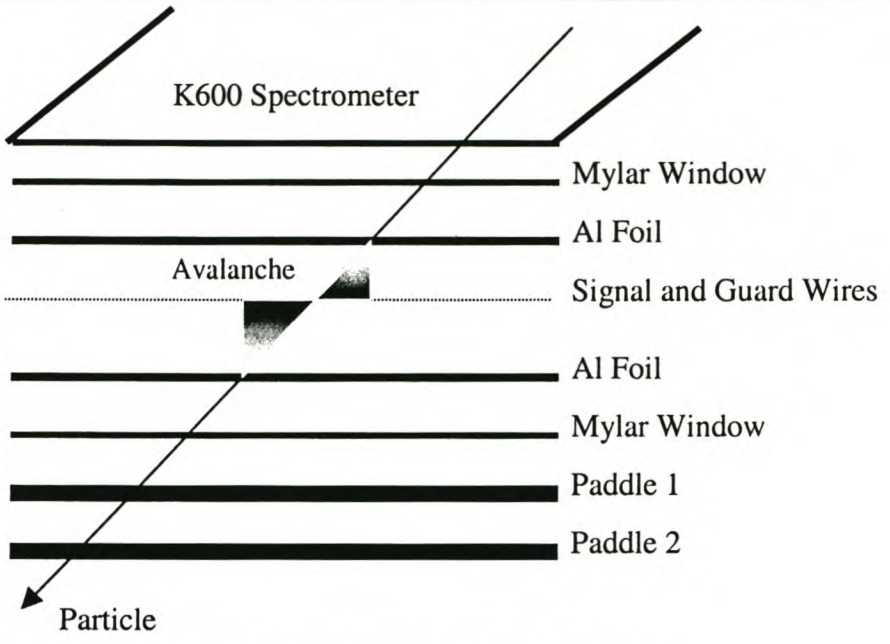

Figure 2.4: The Vertical Drift Chambers

2.7 Plastic Scintillation Detector

There are two plastic scintillation detectors behind the VDC, which are, referred to as paddle 1 and paddle 2. Each of these scintillation detectors has two photomultiplier (PM) tubes connected to it on either end. The scintillation detectors are used for the stop signal of the process, or a so-called event, to indicate when the particle enters the VDC (see section 2.9.2). These start and stop signals are then used to calculate the drift time of the electrons in the VDC. The paddles are operated between +1400 V and +1600 V.

2.8 ΔE-E Telescope

A ΔE-E detector telescope was used in coincidence with the magnetic spectrometer. This detector consisted of a 1 mm thick silicon (Si) surface–barrier detector followed by a 15 mm thick germanium (Ge) scintillation detector. The Si surface barrier detector measured the partial energy loss of an energetic proton, whereas a Ge detector measured the total energy of a proton that stops in the Ge detector. The total energy could then be calculated by adding the energy lost in the Si detector (ΔE) to the energy measured in the Ge detector (E). By

plotting the energy loss characteristics ΔE as a function of E and selecting the locus with protons, particle identification was achieved.

2.9 Electronics

Whereas the electronics to process the fast signals of the VDC and the paddles were located in the spectrometer vault, all the remaining electronics for processing of signals were placed in the data control room at NAC for ease of access and adjustment. The electronics adhered to either the standards of Computer Automated and Control (CAMAC) or Nuclear Instrument Module (NIM). The functions of the electronic modules are discussed in the following paragraphs.

2.9.1 Paddle signals

A flowchart is shown in *figure 2.5*. Each of the two paddles has two photo tubes and the output of these tubes, each fed into a linear fan in. The signals in the fans are then split in two. One signal going to a Constant Fraction Discriminator (CFD) and the other is delayed and then sent to an Analogue-to-digital Converter (ADC). The ADC is used to obtain information on the pulse height of the signal. The output from the CFD for each paddle is combined in a mean timer and the two signals from the mean timers (paddle 1 and paddle 2) are then fed into a four-fold logic unit (4-FLU). If paddle 1 and paddle 2 are in coincidence, the signal is denoted as an event, referred to here as a valid coincidence event A. This signal is then sent to the data control room and tested for coincidence with the telescope event. If an event A and the telescope event are in coincidence it is here referred to as a valid coincidence event B.

One of the signals of the 4-FLU is sent to a time-to-digital converter (TDC) as a start signal for the time of flight (TOF) measurements of the particle in the spectrometer. A signal from the 4-FLU is also sent to another 4-FLU. This 4-FLU tests for coincidence with the RF-signal from the cyclotron. The output of this 4-FLU is used as a stop signal on the TDC. To calculate the drift times in the VDC, a signal from the paddle 1 paddle 2 coincidence 4-FLU is fed via a discriminator to the TDC controller and the experimental common stop for the VDC is obtained.

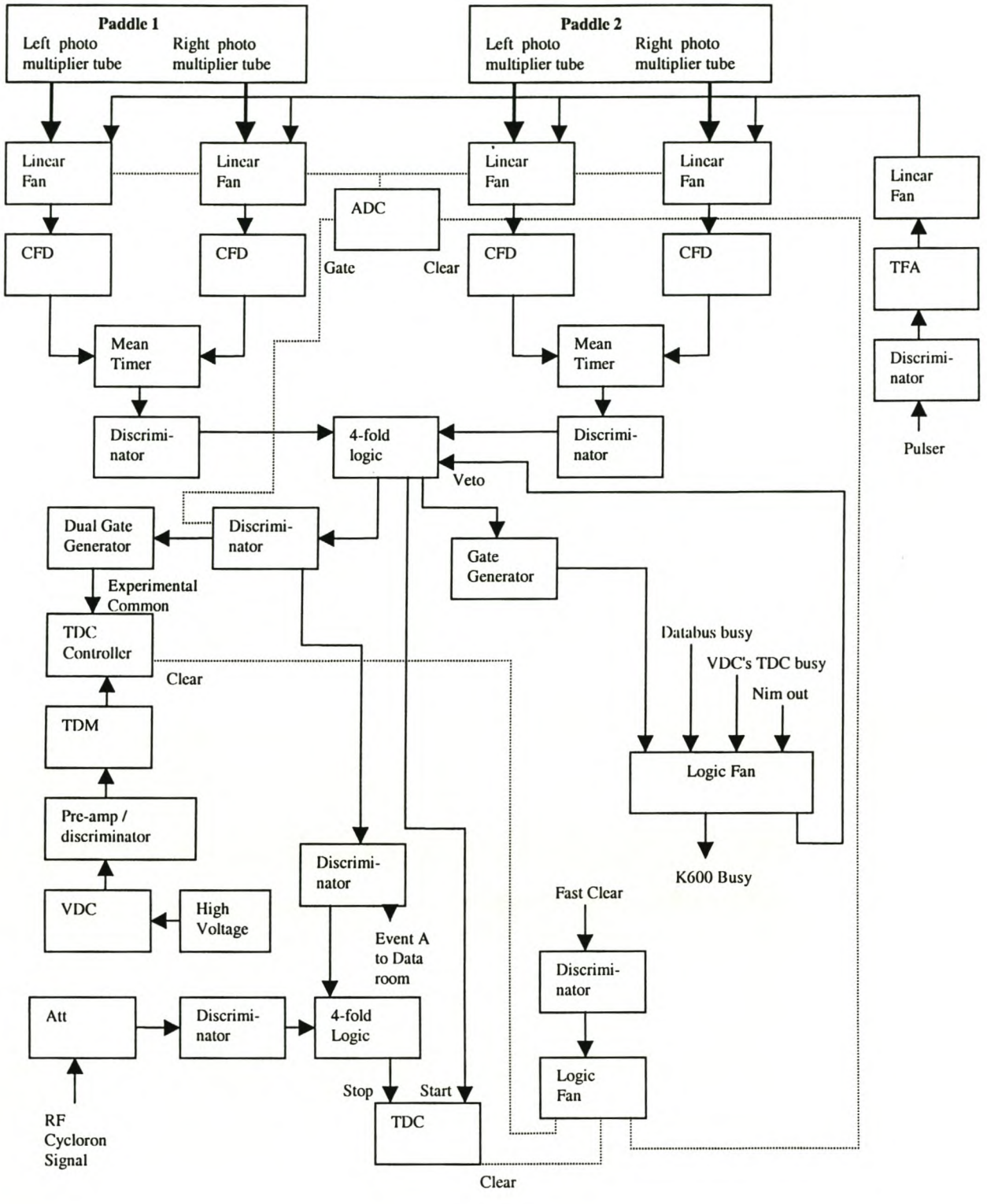

Figure 2.5: Schematic representation of the logic electronics used to process the paddle and VDC signals

2.9.2 VDC signal

The VDC is an array of wires each having its own electronic control. From each wire, the signal goes to a 16-channel VDC mounted preamplifier/discriminator (A/D) card. The separate signals are then combined in seven 32-channel time digitizer modules (TDM). The timing measurement for the delay time calculations are started on receipt of a wire signal and stopped on receipt of the experimental common signal. The experimental common signal is the output pulse of the 4-FLU that is delayed by 500 ns. The valid data is then sent to the memory via a dedicated crate controller (DCC) and a fast bi-directional databus. All the signals from the VDC were processed with the dedicated CAMAC data acquisition system.

2.9.3 Telescope linear signal

A schematic representation for the linear circuit of the ΔE and E detectors is shown in *figure 2.6*. If a signal was received from the silicon (ΔE) or the germanium (E) detectors it was split into two. The first part was used to determine information about the energy that was deposited in the detector. Dedicated preamplifiers amplified these signals. The signals were then sent via the patch panel to amplifiers and delay amplifiers in the data control room. After the delay amplifier, the signal was fed into a linear gate and stretcher (LGS) where a logic signal was required to open the gate in the case of a coincidence event between the ΔE and E detector. The corresponding event signal identified it as an event B, and the linear signal was converted by ADC's and stored as data.

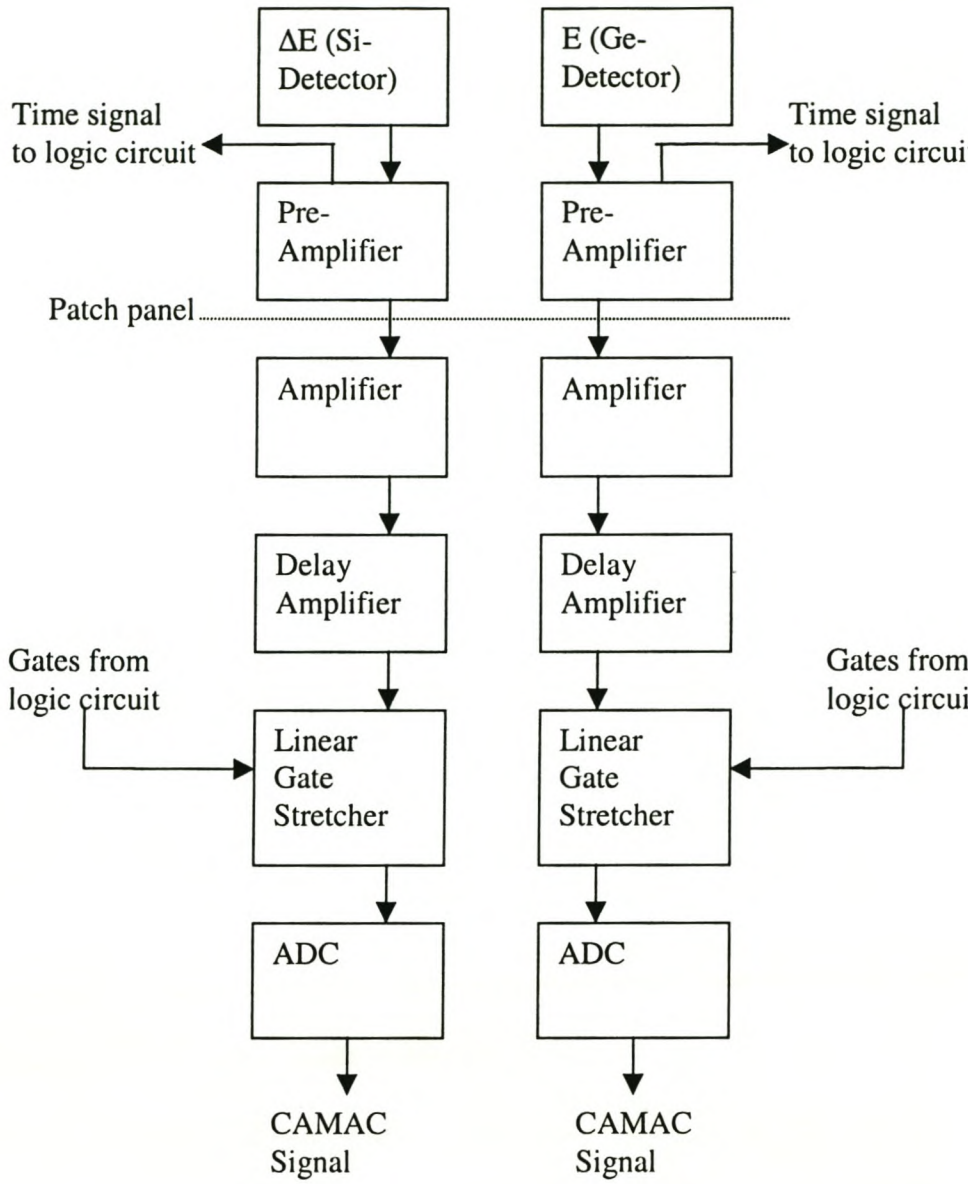

Fig 2.6: Schematic representation of the linear circuit electronic of the ΔE and E detectors

2.9.4 Timing signal

The following timing signals were processed in the data control room. The timing signals from the telescope (see *figure 2.6*) were tested for coincidence. Event B from the telescope and event A from the spectrometer (see *figure 2.5*) were fed into a 4-FLU used as two-fold in coincidence mode.

The spectrometer signal (event A) is wide whereas the telescope signal pulse (event B) is narrow. If telescope signal overlaps with the spectrometer signal pulse, the data is stored as a valid event. But if the separation between two spectrometer signals is less than the pulse width of the spectrometer, it has the effect that accidental coincidence events might be measured in the 4-FLU mentioned in the previous paragraph.

The separation of prompt and accidental coincidences was achieved by making use of the telescope and spectrometer event signals. A time-to-analogue converter module (TAC) generated a coincidence-timing spectrum. All of the peaks in the spectrum contained accidental events, but one prompt coincidence peak also contained real coincidence events. By subtracting accidental event counts from the real coincidence counts, the result is only the number of real events.

2.9.5 Dead time measurement

The computer dead time is measured with the help of a pulser that is combined with the busy signal from the spectrometer. The pulser signal is split in two with the help of a discriminator. One signal served as an uninhibited input to a CAMAC scalar module, while the other output was sent to a 4-FLU. The 4-FLU was used in two-fold, in coincidence with a busy signal from the spectrometer. Thus the pulser was inhibited whenever the spectrometer was busy and this signal formed the CAMAC inhibited signal. By calculating the difference between the inhibited and uninhibited signals, the computer dead time of the spectrometer could be calculated.

2.9.6 Current integration

The current from the beam stop was sent through to the data control room, where it was fed to the current integrator (CI). The CI linearly associates a number of pulses per second to a certain current measured, the full-scale being 1000 pulses per second. A digital output is then split in two with the help of a discriminator. The one signal served as a uninhibited input to a CAMAC scalar module, while the other output was sent to a 4-FLU. The 4-FLU was used in two-fold with coincidence with a signal from the spectrometer busy signal. Thus the signal from the CI was inhibited whenever the spectrometer was busy, and this signal corresponded to the CAMAC inhibited signal. As reference, the other signal was registered as a CAMAC uninhibited signal.

2.10 Data Handling

2.10.1 Hardware

The data handling hardware consists of NIM modules, four CAMAC crates and a VME front-end. The data is transferred from the NIM's via the four CAMAC crates, two of which are in the spectrometer vault and the other two in the data control room, to the VME front-end. The VME is the interface to the VAX data computer and this dedicated VAX did the online data handling analysis. For further information on the VME see [Yod94] and [Pil96].

2.10.2 Software

All the software used to control data is from the system XSYS, which runs on the VAX VMS operating system platform. In XSYS, two program files are run to handle data, namely the COM file and the EVAL file.

The COM file creates all the necessary data areas for the data to be stored (this includes data areas for gates and graphs). The EVAL code uses these data areas to sort and analyse the raw data from the buffers. This raw data is stored on magnetic tape in data files and these data files can be played back with various software gates and offline sorting routines at a later time to analyse data, by using the same COM and EVAL files.

The EVAL file also does verification and analysing of events. The EVAL code tests for coincidence between the VDC paddles and the telescope detectors. The EVAL code also does the calculation to determine the energy associated with a specific position in the VDC of the K600. This program also calculates the energy and recoil momentum for each event.

2.11 Experimental Procedure

As was already mentioned, the experiment ran over four weekends, but the experimental data was collected on the last three of these weekends. On the first weekend all the energy resolutions and settings were determined. For these calibrations and initial set-up a Si/NaI (ΔE-E telescope) detector was used instead of the Si/Ge (ΔE-E) detector. The energy

resolution of the germanium detector was checked beforehand with the gamma spectrum from a ^{152}Eu source.

The response time of the different wires in the VDC was set first. Differences in the lengths of cable that connect the TDM's with the A/D cards and variations in the VDC-mounted A/D cards caused differences in response times of different VDC wires. Therefore the TDC were trimmed such that all the effective response times were the same.

With the help of a ruby crystal, the beam was positioned on the target. The beam halo was checked with the empty frame position in the target ladder. Proper set-up was achieved by sending the beam through this empty position in the ladder and tuning the proton beam until the count rate in the paddles was a minimum. A $(CH_2)_n$ target was used in the high energy beam line to determine the polarisation of the beam.

The field settings for the dipole magnets and the high voltages of these coils were set from the data control room. The setting of these coils ensured that particles of a specific energy travel along the central-momentum trajectory of the K600 spectrometer. The ^{12}C target was used to do an energy calibration on the magnetic spectrometer.

The lookup table (see Chapter 3.4.1), that was needed for the purpose of determining the position of particles in the focal plane, was produced from the average VDC drift-time spectrum that is associated with inelastic scattering of protons from the ^{12}C target.

The K600 spectrometer resolution was optimised with a $(CH_2)_n$ target. This was done by plotting the Time-of-Flight (TOF) of a scattered proton through the K600 as a function of the position on the focal plane. The resolution was then optimised by adjusting the K-and H-coils.

The ^{208}Pb experimental runs typically lasted 2 hours and they were alternated with $(CH_2)_n$ runs to determine the beam polarisation. The data from these runs were all acquired with XSYS, as the COM and EVAL file were executed in real time while the experiment was in progress. During these runs the VDC efficiency was also checked and increased by setting

the high voltage on the high voltage cathode planes of the VDC. The VDC efficiency ranged between 93% and 95%.

Chapter 3: DATA REDUCTION AND ENERGY CALIBRATION

3.1 Overview

In this chapter the techniques that were used to extract the data are discussed. Some of the methods were programmed in the EVAL code and applied whilst acquiring the data. Other analyses were done with the help of various programs such as, KINMAT, ELOSS and PLOTDATA. Three PASCAL programs were developed to calculate the experimental cross-section and experimental analysing power. Another two PASCAL programs were used for the theoretical calculations; these are discussed in Chapter 4.

In the first section, the energy calibrations of the K600 spectrometer and the germanium detector are discussed. The following sections discuss the different techniques that were employed to identify the different particles emerging from the interaction of protons with ^{208}Pb; in this experiment protons were identified and selected. In section 3.4 all corrections that were applied to the data are discussed. In section 3.6 an overview is given of the analysing power calculations and the measurement of the polarisation of the beam is also explained. Section 3.7 describes calculations that were performed to obtain the absolute cross-section.

3.2 Energy Calibrations

3.2.1 K600 Spectrometer

The relation between momentum (p) and kinetic energy (T) of a particle at relativistic velocities is given by

$$p = \frac{\sqrt{T^2 + 2Tm_0}}{c}, \qquad (3.1)$$

where m_0 is the rest mass energy of the particle [Fra91]. *Table 3.A* lists the measured incident kinetic energy, determined by time of flight along the beam line, marked X in *figure 2.1*, and the calculated momentum of the incident protons.

The momentum of a particle entering the K600 spectrometer determines the path that the particle follows in the magnetic field of the spectrometer. The position where the particle hits the focal plane is related to the path that was followed, and from this position the momentum of the particle, can be calculated. In terms of the central momentum (p_c), the momentum calibration (p) of the focal plane position (x) can be expressed as

$$\frac{p}{p_c} = k_x(x) + k_0, \qquad (3.2)$$

where k_x and k_0 are the calibration constants, as they were used in the EVAL code for x in terms of channel numbers as defined by the data acquisition software.

The calibration was achieved with elastic and inelastic scattering of protons from ^{12}C at a specific scattering angle. The first three states of ^{12}C were utilised for calibration, namely the ground state (0.0 MeV), first excited state (4.4 MeV) and second excited state (9.64 MeV). Each of the three weekends, over which the experiment was conducted, was started with a run on ^{12}C, for the calibration of the K600. Three peaks in the energy spectrum, associated with the three excited states of ^{12}C, were visible. The energy values at the centres of these three peaks in the energy spectrum were then used with the kinematics computer program KINMAT to calculate the calibration values. The calibration values k_x and k_o (see *table 3.A* for the results) were determined with a linear curve fit using the central momentum trajectory.

3.2.2 Silicon detector (ΔE)

The silicon detector was not calibrated in this experiment, as the energy lost in the silicon was small in comparison to the total energy of the proton. (This loss of energy was treated on a similar footing as the losses due to dead layers in front of the Ge detector.) The precise energy loss for the silicon detector, of which the thickness was known accurately (1000±3 μm), was calculated with the computer program ELOSS. This calculation is discussed in paragraph 3.2.3 and paragraph 3.4.4.

The elastic and inelastic scattering of protons from ^{12}C could not be utilised to calibrate the germanium detector, because the maximum energy that the 15 mm detector can measure is 78 MeV, as calculated with the program ELOSS. Therefore if the energy of the incoming proton is 81 MeV, the proton will loose 1.6 MeV in the silicon detector, bringing the total

energy observed in the silicon- and germanium-detectors to 81 MeV. Consequently this is the maximum energy that the ΔE-E telescope could measure, with protons of higher energy punching through the germanium detector. Such events will have a signal from the silicon detector corresponding to the correct ΔE value, but the germanium detector will measure a lower energy for the particle. The event will consequently not be on the ΔE-E locus of the protons and will be excluded from the PID software gate. *Figure 3.1* shows clear evidence for such a locus below the gate area.

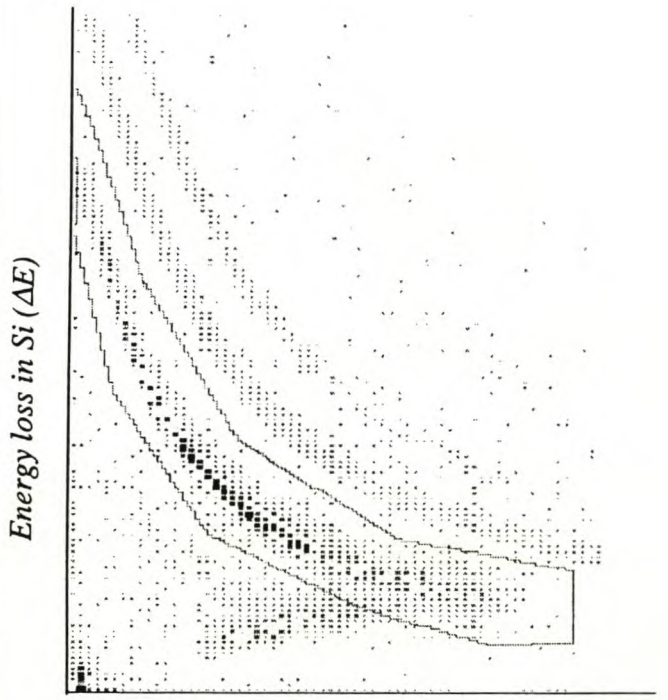

Figure 3.1: A telescope particle identification spectrum (PID)

3.2.3 Germanium telescope (E)

The $^{1}H(p,p)^{1}H$ elastic scattering was used for this energy calibration. The germanium calibration was done after the K600 spectrometer was calibrated. The energy of the one scattered proton from the $^{1}H(p,p)^{1}H$ elastic reaction can be calculated if the energy of the other proton and the incident energy are known. Therefore, as the incident energy and the energy of the proton in the calibrated spectrometer were known, the energy of the proton in the germanium detector could be calculated. The method therefore consisted of observing the scattered proton from $^{1}H(p,p)^{1}H$ elastic scattering in coincidence with the recoil target proton

in the germanium detector. In the EVAL code the calibration was assumed to be linear and given by

$$E_p = k_N^g \times (N) + k_0^g , \qquad (3.3)$$

where N is the channel number where the peak is located in the energy spectrum of the telescope, E_p is the energy deposited by the particle and k_N^g and k_0^g are the calibration constants. The electronics were also adjusted beforehand, so that zero energy coincides with the zero channel in the analyser, thus having the effect that $k_0^g = 0$. Subsequently changing the calibration variable k_N^g, so that the width of the "hydrogen peak"[⊕] was a minimum, refined the calibration. These values for the three weekends are tabled in *table 3.A*.

Table 3.A: The calibration values for the K600 Spectrometer and the Ge detector.

	Beam Kinetic Energy (MeV)	*Beam Momentum (MeV/c)*	k_x (x 10^{-5})	k_o (x 10^{-1})	p_c *(fieldset)*	k_N^g (x 10^{-2})
Weekend 1	200.9	646.1	2.282	9.325	539.4	1.215
Weekend 2	200.5	645.4	2.258	9.363	576.6	1.170
Weekend 3	200.2	644.9	2.274	9.386	504.4	1.150

3.3 Particle Identification

3.3.1 Particles in the telescope

In the telescope the particles lost some energy in the silicon detector (ΔE) and the remainder in the germanium detector (E). According to the Bethe equation the amount of energy that a particle loses in a medium, is given by the following relation [Kno89]

$$-\frac{dE}{dx} \propto \left(\frac{q}{v}\right)^2 , \qquad (3.4)$$

[⊕] The peak corresponding to events from $^1H(p,p)^1H$ elastic scattering as a function of the summed energy

where q is the charge and v the velocity of the particle. As the charge of different particles differ from each other, the energy loss in the medium will differ. By plotting the energy loss in the silicon detector (ΔE) as a function of the energy loss in the germanium detector (E), a so-called particle identification spectrum (PID) can be obtained. A typical PID is illustrated in *figure 3.1*. By choosing a software gate around the locus of the protons (as shown in *figure 3.1*), they could be selected for further data sorting.

3.3.2 K600 Spectrometer

Two techniques were employed simultaneously for particle selection in the spectrometer. In the first of these the two paddles operate in a way analogous to the two detectors in the telescope (ΔE-E). A PID of the two paddles was then plotted and the proton locus was selected with a software gate (a typical PID with the software gate on the protons is shown in *figure 3.2*).

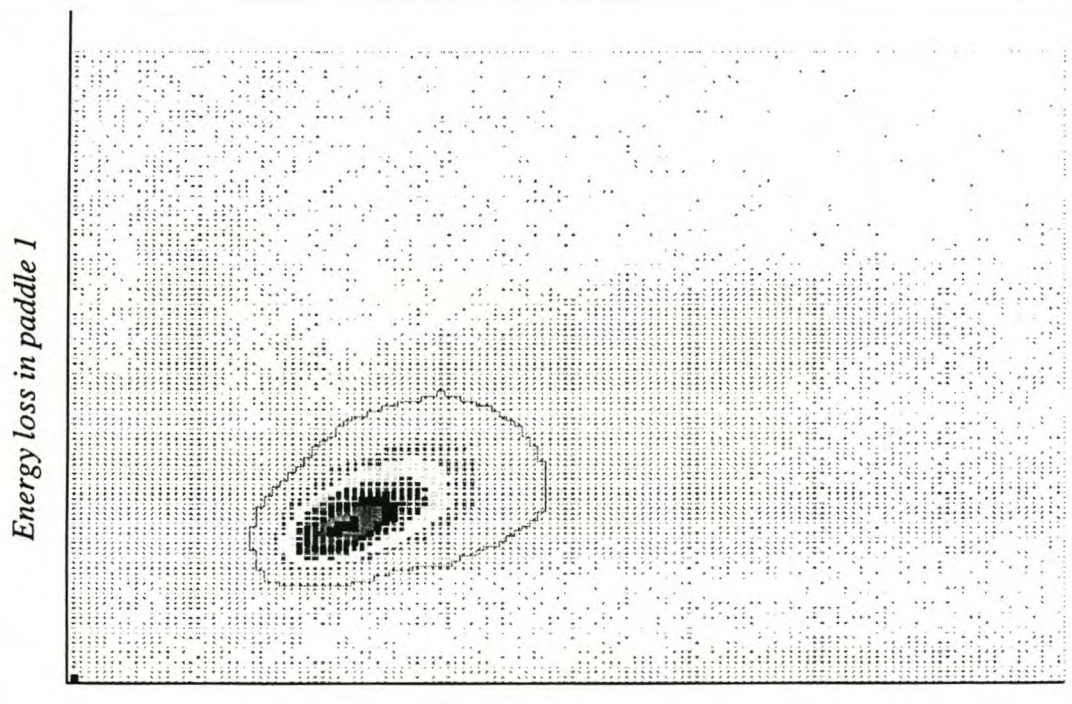

Figure 3.2: A particle identification spectrum for the K600 (PID)

In the second process a time of flight (TOF) spectrum was used. As the mass of different particles differ, so will the flight times of these particles differ in the magnetic field of the

spectrometer; for the same value of p/q different particles will end up at the same position in the focal plane. By plotting a TOF spectrum (time of flight relative to the phase of the cyclotron RF) and setting a software gate, the protons can then be selected. An example of a TOF spectrum with the software gate set on the proton peak is illustrated in *figure 3.3.*

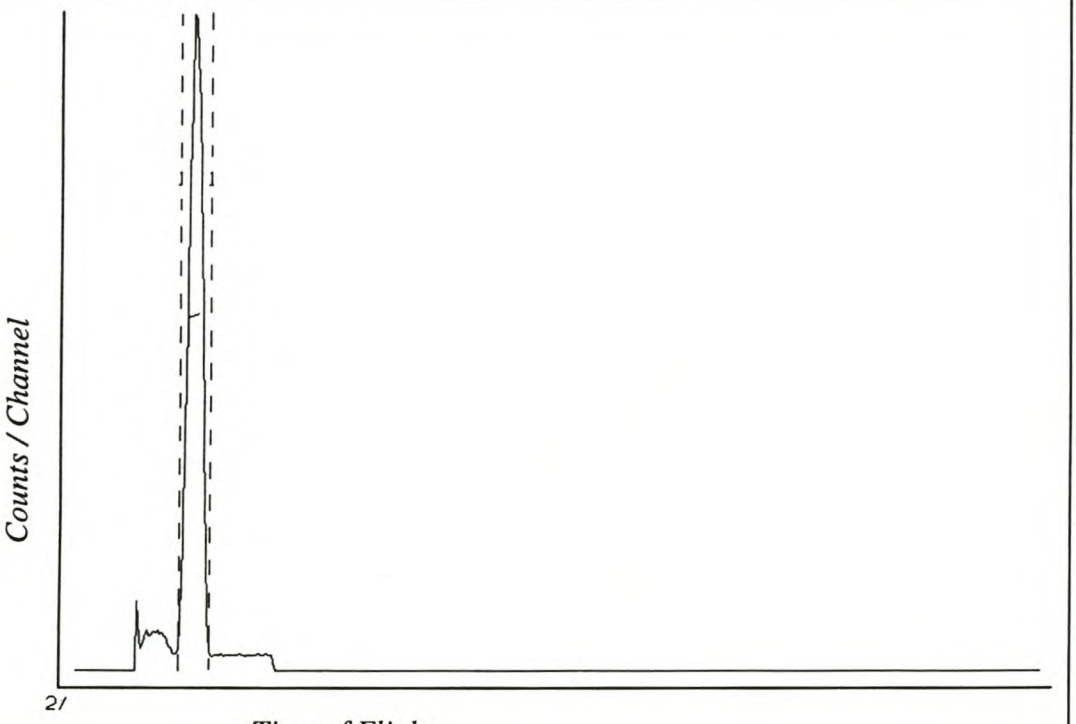

Figure 3.3: A Time of Flight spectrum (PID)

3.4 Correction in the Data Analysis

3.4.1 Lookup tables for the VDC

To determine where a particle went through the VDC a so-called lookup table needs to be generated. The spectrometer paddles register particles without an appreciable time delay, but in the VDC the particles are registered with a time delay. This time is known as the drift time and is proportional to the distance that the particle passed from a signal wire in the VDC, as the electrons has to drift from the particle's path to the closest signal wires.

By scattering 200 MeV protons inelastically with large energy loss as selected by the momentum range of the magnetic spectrometer, from a ^{12}C target, the VDC is uniformly

illuminated and all possible drift times are measured. The average of all these drift times from all the signal wires then creates a so-called 'white spectrum'. A computer program, LUT.PCM, then relates the drift time to a drift distance and stores this data in a lookup table.

The drift distance, obtained from the lookup table, combined with the signal wires that fired is then used to calculate the precise position where the particle crossed the VDC. This is done to an accuracy of 0.3 mm, giving an energy resolution of about 8 keV [Nev98]. Lookup tables were generated for each of the three weekends.

3.4.2 Shift of the lookup tables

It is impossible for the electronics, associated with the VDC, to measure a zero drift time. To correct this, the lookup table needs to be shifted. This shift was done similar to the shift for the experiment that was conducted at the National Accelerator Centre (NAC) during August 1997 [Nev98].

3.4.3 VDC efficiency

The VDC efficiency (ε) can be defined as the product of the geometric efficiency (ε_g) and the intrinsic efficiency (ε_i) [Kno89; Leo84].

$$\varepsilon = \varepsilon_g \varepsilon_i . \qquad (3.5)$$

The geometric efficiency was previously checked with a horizontal drift chamber and found to be very close to unity [New96]. The geometric efficiency was thus taken as 100% in this work. The intrinsic efficiency (ε_i) was calculated by dividing the number of valid events (N_{valid}) that were accepted by the EVAL code, by the total of all the events (N_{total}) that were registered by the VDC as counted on a scaler.

$$\varepsilon_i = \frac{N_{valid}}{N_{total}} \qquad (3.6)$$

The valid event in the VDC was calculated with the following equation

$$N_{valid} = N_{total} - (N_{max} + N_{min} + N_{drift} + N_{group}) \qquad (3.7)$$

Where N_{max} is the number of events where more than eight signal wires fired.

N_{min} is the number of events where less than three signal wires fired.

N_{drift} is the number of events where the drift times were too long.

N_{group} is the number of events where no grouping could be formed.

An extensive discussion of this method can be found in [Nev98]. The VDC efficiencies for the different weekends are listed in *table 3.B*.

Table 3.B: The VDC efficiencies for the different weekends.

	Fieldset	*VDC efficiencies (%)*
Weekend 1	2	92
Weekend 2	3	93
Weekend 3	1	94

3.4.4 Energy correction due to the dead layers

Several materials reduced the energy of the proton before it was measured in the germanium crystal. These materials were in position between the germanium crystal and the target and were:

a. 75 μm Kapton (exit window of the target camber).

b. 6 cm of helium placed between the exit window and the detector (to reduce scattering of protons from air).

c. 1000 μm of silicon (ΔE-detector).

d. 125 μm beryllium (entrance window for the germanium detector).

The energy losses through the Kapton, helium and beryllium were calculated with the program ELOSS. The energy loss in the silicon was calibrated with the use of an α-source, in this case ^{228}Th. The energy losses in the Kapton, helium and beryllium were then added and treated as a dead layer energy loss (E_{dead}). This calculation was done for ten different incident energies. The ten different dead layer energy losses were then plotted against the different energies measured in the germanium detector (E_{Ge}). A curve was fitted to this plot and the following relation was derived

$$E_{dead} = a + b\left(1 + \left(\frac{E_{Ge}}{c}\right)^{d}\right)^{-1} \qquad (3.8)$$

where $a = 0.0984$

$b = 13.9720$

$c = 2.2591$

$d = 1.2652$

A FORTRAN program was written to correct the measured energies in the germanium detector.

3.4.5 The reaction tail corrections of the germanium crystal

The germanium crystal detector (GCD) relies on elastic collisions between the incoming particles and the atomic electrons, to determine the particle energy. In these elastic collisions all the energy of the particle (mainly protons in this experiment) is eventually deposited in the crystal before it stops, with the effect that the total energy of the particle can be measured. The incoming particle can, however, also be involved in inelastic nuclear reactions with the formation of a neutral reaction product that carries away some energy that is not deposited in the detector. All energy transferred in an inelastic reaction may therefore not be detected and the final measured energy of the particle then appears to be less than the real initial energy of the particle. These events of lower energy are referred to as the reaction tail of the full energy peak. Because any particle that is affected by these reaction tail processes would be registered with an erroneous energy value, it will fall outside the events included in the gate region. The percentage loss due to this effect for different energies is tabulated in *table 3.C* [MeaA69].

Table 3.C: The Percentage interaction loss in germanium.

Energies (MeV)	*Particles lost (%)*
30	1.3
40	2.2
50	3.2
75	6.0
100	9.0
125	12.6

The maximum energy of the incoming protons of interest in the telescope, was approximately 75 MeV. After energy loss in the dead layers, the energy of the particle would be between 70 MeV and 72 MeV. For these energies the loss, because of reaction tail interaction, would be less than 6% (see *table 3.C*), and typically about 2%. This effect was neglected for the experiment because of the low average percentage loss.

3.4.6 Electronic dead time

No correction was applied for the electronic dead time, also known as the spectrometer dead time (see section 2.9.5). This dead time was however taken into account in the error analysis (see section 3.4.7).

The computer dead time correction was automatically performed by the hardware. The ratio between the current inhibited and current uninhibited signals resulted in the correction factor (see section 2.9.5).

3.4.7 Systematic errors

The systematic errors, that influenced the differential cross-section, are listed in the table below (*table 3.D*). The combined errors were estimated from these errors and found to be of the order of 9% [Nev98].

Table 3.D: The list of systematic errors.

Sources of systematic errors	*Magnitude of the Errors (%)*
Target Thickness [Ard97]	7
K600 solid angle [New96]	0.3
Ge detector solid angle [For92]	1
Particle Identification [MEA69]	6
Electronic Dead time	2
Total Systematic Error	9

3.5 Projection Spectra

After all the corrections mentioned so far were taken into account, projection spectra were plotted to extract the necessary data for the calculation of the binding energy. A spectrum of the energy measured in the telescope is then plotted against the energy measured in the K600. This clearly shows the loci of the hydrogen and that of the knockout reactions. This spectrum is shown in *figure 3.4* with the more extended locus being that of the knockout reactions in lead.

The total energy (energy measured in the telescope and the K600) is then plotted against only the energy measured in the K600 as a consistency check on the calibrations. In this spectrum (*figure 3.5*) two knockout peaks could be identified. The final spectrum (*figure3.6*) is the binding energy spectrum (counts vs. total energy, given in terms of channel number) that shows the two peaks. On this spectrum the gates are set as to extract the final data for the different binding energy states.

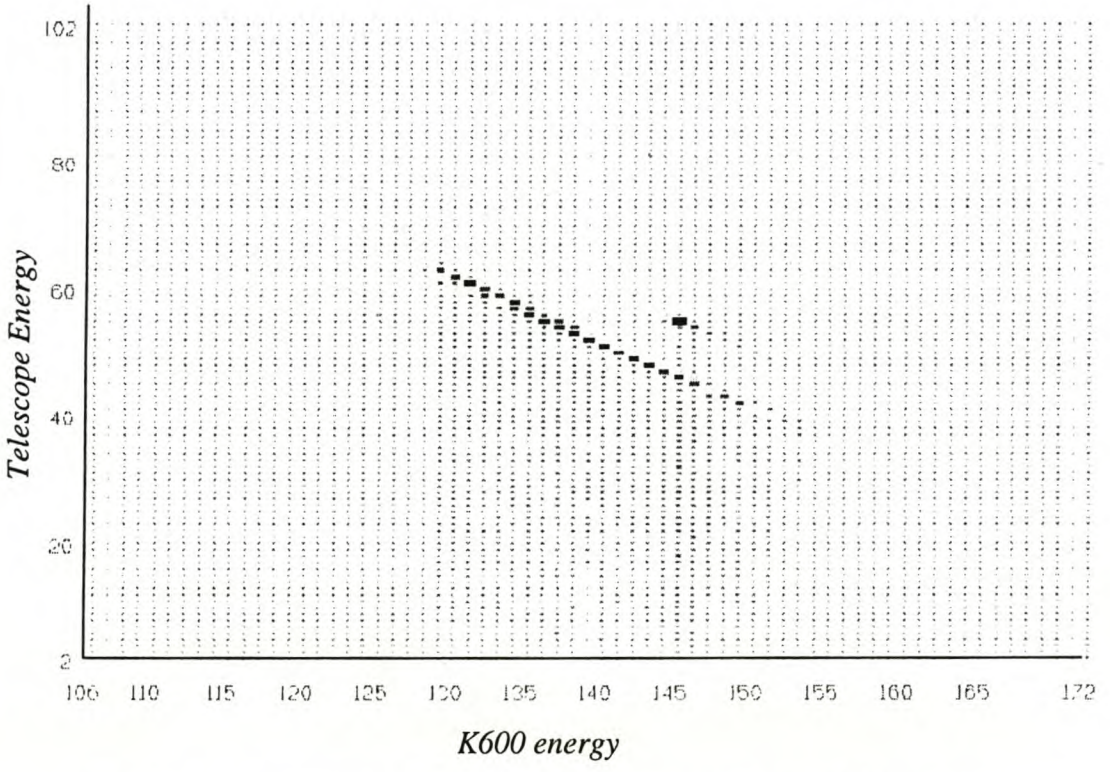

Figure 3.4: A spectrum of the telescope energy versus the K600 energy

The absolute cross-section was calculated out of the binding energy spectrum for data measured during each weekend. The typical binding energy spectrum (see *figure 3.6*) had three peaks. The peak on the far right hand side of the spectrum is the peak due to hydrogen contaminant in the lead target. Two software gates are set over the two peaks corresponding to knockout of protons from lead, on the left of the graph. These two knock out peaks each contain two of four energy states ($3s_{1/2}, 2d_{3/2}, 1h_{11/2}, 2d_{5/2}$). The larger peak contains the ground state and the first excited energy states (being $3s_{1/2}$ and $2d_{3/2}$ respectively) and the

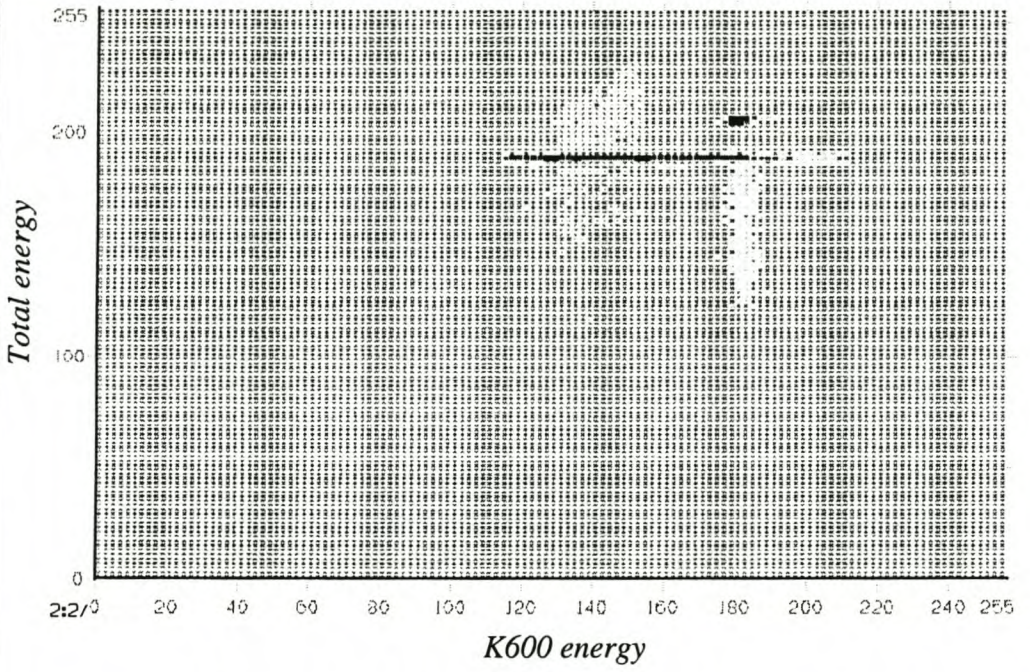

Figure 3.5: The total energy versus the K600 energy in MeV

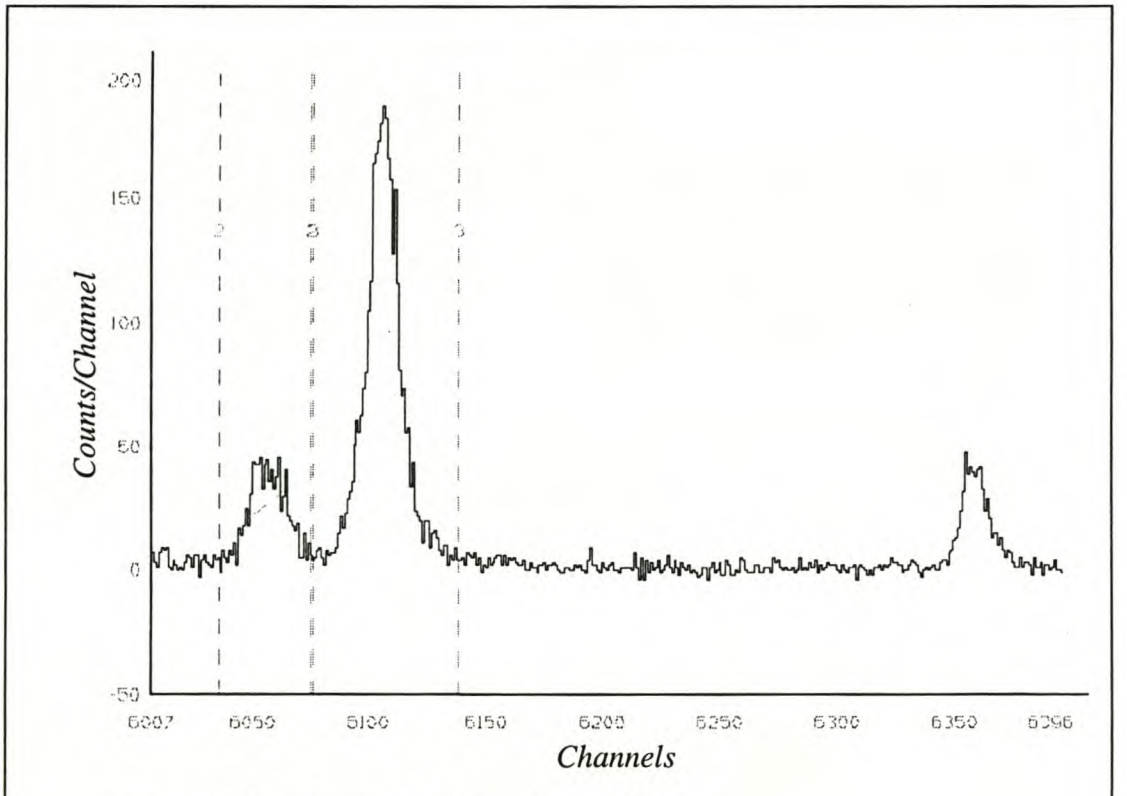

Figure 3.6: A typical binding energy spectrum

smaller peak the two higher states (being $1h_{11/2}$ and $2d_{5/2}$ respectively). The counts per channel were extracted from these spectrums and used to calculate the absolute cross-section.

3.6 Analysing Power

3.6.1 Measurement of the incident polarisation

The polarisation of the incident beam was measured with a polarimeter, which was placed in the high-energy beam line *P1* (see *figure 2.1*). The polarimeter has two detectors at scattering angles of 18° on opposite sides of the incident beam that measure the number of events left that have spin-up ($L\uparrow$) and spin-down ($L\downarrow$) and the number of events right that have spin-up ($R\uparrow$) and spin-down ($R\downarrow$). A polarisation run was conducted every two hours during the experiment, by means of an elastic scattering reaction of protons on ^{12}C. The analysing power of this reaction is known to be [Li94]

$$A_y = 0.98. \qquad (3.9)$$

From the following equation, at an angle of 18°, the values for polarisation-up ($p\uparrow$) and polarisation-down ($p\downarrow$) can then be calculated [Hae74].

$$p_\uparrow = \frac{\varepsilon_\uparrow}{A_y}, \qquad (3.10)$$

where

$$\varepsilon_\uparrow = \frac{L_\uparrow - R_\uparrow}{L_\uparrow + R_\uparrow}$$

and

$$p_\downarrow = \frac{\varepsilon_\downarrow}{A_y}, \qquad (3.11)$$

where

$$\varepsilon_\downarrow = \frac{L_\downarrow - R_\downarrow}{L_\downarrow + R_\downarrow}.$$

The average percentage values for the beam polarisation are given in *table 3.E.*

Table 3.E: The Average Beam Polarisations for the different weekends.

	Polarisation Up $(p_\uparrow)$ *(%)*	*Polarisation Down* $(p_\downarrow)$ *(%)*
Weekend 1	74	71
Weekend 2	76	64
Weekend 3	61	67

3.6.2 Analysing power calculations

The coincidence yields $C\uparrow$ and $C\downarrow$, for both spin-up and spin-down (denoted by $\uparrow,\downarrow$ respectively) are proportional to the cross-section $d^3\sigma_\uparrow$ and $d^3\sigma_\downarrow$, and are expressed as [Hae74].

$$d^3\sigma_\uparrow \propto C_\uparrow = I_0\left(1 + p_\uparrow A_y\right) \qquad (3.12)$$

and

$$d^3\sigma_\downarrow \propto C_\downarrow = I_0\left(1 - p_\downarrow A_y\right), \qquad (3.13)$$

where A_y represents the analysing power of the $\left(\vec{p},2p\right)$ reaction, $p\uparrow$ and $p\downarrow$ represent the spin-up and spin-down beam polarisation and I_0 is the coincidence yield at the same kinematics but with an unpolarised beam. The following equation can be derived from these two equations

$$A_y = \frac{C_\uparrow - C_\downarrow}{C_\uparrow p_\downarrow + C_\downarrow p_\uparrow}. \qquad (3.14)$$

This equation was used to calculate the analysing power for the final results. If $p=p\uparrow=p\downarrow$ the equation can be simplified to

$$A_y = \frac{C_\uparrow - C_\downarrow}{p\left(C_\uparrow + C_\downarrow\right)}. \qquad (3.15)$$

For comparison, calculations for the analysing power were also done with this equation, and the results were comparable to results of the previous method. This reflects that $p\uparrow \approx p\downarrow$, as listed in *table 3.E.*

3.6.3 Statistical error

The statistical (σ) error on the content of each of the energy bins is

$$\sigma = \sqrt{N}\,, \qquad (3.16)$$

where N is the number of counts in each bin [Kno89]. The error propagation formula [Kno89] can then be applied to the equation that was used to calculate the final analysing power (A_y) and the statistical error (σ_{A_y}) can then be determined with

$$\sigma_{A_y}^2 = \left(\frac{\partial A_y}{\partial C_\uparrow}\right)(C_\uparrow)^2 + \left(\frac{\partial A_y}{\partial C_\downarrow}\right)(C_\downarrow)^2 . \qquad (3.17)$$

Simplifying this gives

$$\sigma_{A_y} = \left[\frac{1}{(C_\uparrow p_\downarrow + C_\downarrow p_\uparrow)^2}(C_\uparrow + C_\downarrow)^2 + \frac{(C_\uparrow - C_\downarrow)^2}{(C_\uparrow + C_\downarrow)^4}(C_\uparrow p_\downarrow^2 + C_\downarrow p_\uparrow^2)\right]^{\frac{1}{2}} . \qquad (3.18)$$

This equation was used to calculate the errors on the analysing power. Using the numerical data, in this equation, it was found that the second term in the bracket could be neglected in relation to the first term.

3.7 Absolute Cross-section

As mentioned earlier the absolute cross-section was calculated for the binding energy spectrum for each weekend. The one peak contained the ground state and the first excited energy state ($3s_{1/2}, 2d_{3/2}$) and the other peak contained the two higher states ($1h_{11/2}, 2d_{5/2}$). The counts for each weekend were used to calculate the absolute cross-section.

The absolute cross-section (in mb.MeV^{-1}.sr^{-2}) is given by [For92]

$$\frac{d^3\sigma}{d\Omega_1 d\Omega_2 dE} = \frac{N_c.10^{27}}{\Delta\Omega_1.\Delta\Omega_2.\Delta E.N_0.\rho.\varepsilon_{VDC}}, \qquad (3.19)$$

where N_c is the corrected number of counts in an energy bin ($C\uparrow$ or $C\downarrow$),

$\Delta\Omega_1, \Delta\Omega_2$ are the solid angles (in sr) subtended by the K600 spectrometer and the silicon/germanium telescope respectively,

ΔE is the width of the energy bin (in MeV),

ε_{VDC} is the efficiency of the VDC,

N_0 is the total number of protons incident on the target, given by

$$N_0 = \frac{C.R.10^{-12}}{e},$$

where C is the current-integrator-inhibited scaler reading (integrated charge measured by the current integrator when the data acquisition is inhibited by a busy signal),

R is the selected range (in nA) which represents $R.1000$ counts per second for the full scale current readout,

e is the charge of a proton (in Coulomb),

and ρ is the number of nuclei per unit area of ^{208}Pb target (in cm^{-2}) and can be given by

$$\rho = \frac{\lambda.N_A}{A},$$

where λ is the target thickness (in g/cm^2),

N_A is Avogadro's number,

A is the atomic mass of the target (in g/mol).

The statistical error of the absolute cross-section is given by

$$\sigma = \frac{\sqrt{N_c}.10^{27}}{\Delta\Omega_1.\Delta\Omega_2.\Delta E.N_0.\rho.\varepsilon_{VDC}}. \qquad (3.20)$$

These equations were used to calculate the spin-up and spin-down cross-sections and the statistical errors associated with them.

Using the relations as stated in paragraph 3.5.2 [Hae74]

$$d^3\sigma_{\uparrow} \propto I_0\left(1 + p_{\uparrow}A_y\right) \qquad (3.21)$$

and

$$d^3\sigma_{\downarrow} \propto I_0\left(1 - p_{\downarrow}A_y\right). \qquad (3.22)$$

It follows that

$$I_0 = \frac{C_{\uparrow} + C_{\downarrow}}{2 + A_y\left(p_{\uparrow} - p_{\downarrow}\right)}. \qquad (3.23)$$

By converting the unpolarised yield (I_0) with the same conversion factor as for $C\uparrow$ or $C\downarrow$, the cross-section ($d^3\sigma_0$), the equation becomes

$$d^3\sigma_0 = \frac{d^3\sigma_{\uparrow} + d^3\sigma_{\downarrow}}{2 + A_y\left(p_{\uparrow} - p_{\downarrow}\right)}. \qquad (3.24)$$

This equation was used to combine the spin-up and spin-down cross-sections for the final cross-section. As ($p\uparrow$-$p\downarrow$) is generally smaller than 0.1 and $A_y \leq 1$, the cross-section is within a few percent of the average of the spin-up and spin-down values.

The final cross-section was approximated as

$$= \frac{\sigma_{\uparrow} + \sigma_{\downarrow}}{2}.$$

Chapter 4: THEORY

4.1 Overview

In this chapter, the theoretical models that underlie this experiment are discussed. The so-called quasi-free scattering process refers to a projectile that knocks a nucleon out of a nucleus, without any further violent interactions occurring between the projectile and the residual nucleus. For this interaction, incoming protons of a hundred or more MeV are needed and the general form of the nuclear reaction can be expressed as

$$ {}^{A}_{Z}X(p,2p)^{A-1}_{Z-1}Y , \qquad (4.1) $$

where X and Y represent the target and recoil nuclei respectively. The initial model used in this experiment, for the quasi-free scattering process, is based on two assumptions. The first is that the collision time is short and that the collision can be described by an impulse approximation. The second assumption is that there is no interaction between the incoming particles and the target nucleus before the collision; there is also no interaction between the outgoing particle and the residual nucleus after the collision or between the outgoing particles amongst themselves.

These assumptions give rise to the Plane Wave Impulse Approximation (PWIA). As a result of this assumption, not taking into account the interaction between the nucleus and the incoming and outgoing particles, the cross-sections for the knockout reaction are overestimated. The Distorted Wave Impulse Approximation (DWIA) however takes this reaction into account and thus gives more realistic cross-section values for the knockout interaction. The DWIA for quasi-free knockout reactions is accepted as a good model for reactions with incoming energies of greater than 100 MeV. Both these models will be discussed in the following three sections.

The calculations for these theoretical models were programmed by Chant *et al.* [Cha92]. This program, called THREEDEE, was employed for all the theoretical calculations. Two PASCAL programs were also developed to combine the theoretical cross-sections and theoretical analysing power, as well as determining the spectroscopic factors for the different energy states. All these calculations are discussed in sections 4.5 and 4.6.

4.2 Transition Amplitude

Consider the reaction *A(a,cd)B* where *A* is the target nucleus, *a* the incoming proton, *c* and *d* the outgoing protons and *B* the residual nucleus (as shown in *figure 4.1*). The *b* in the diagram indicates a proton bound in the nucleus *A*.

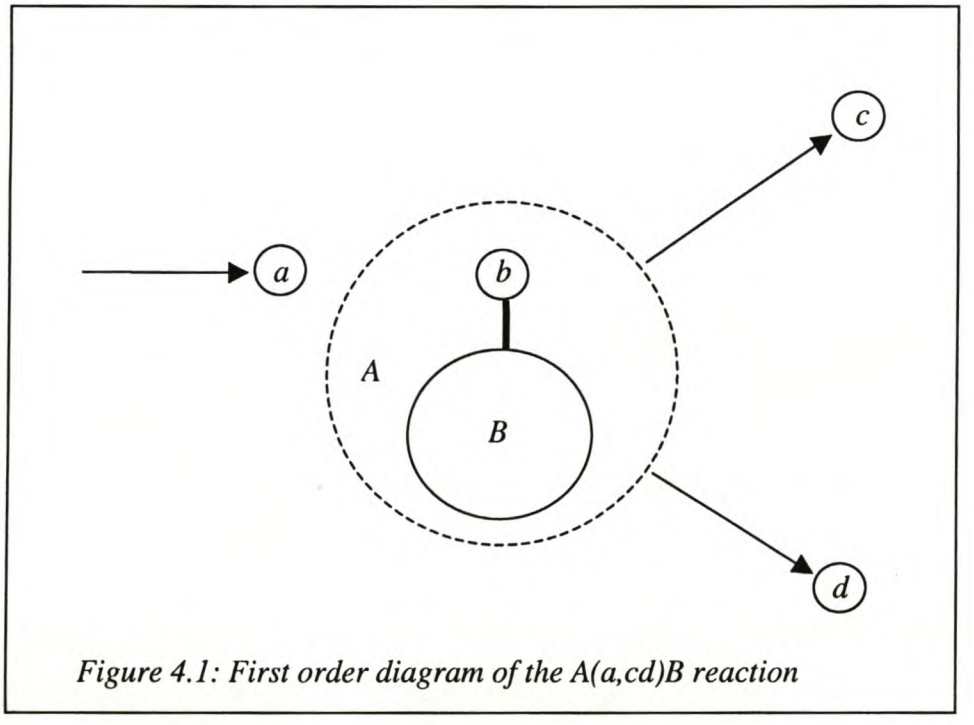

Figure 4.1: First order diagram of the A(a,cd)B reaction

The transition amplitude for this knockout reaction is given by [Cha77]

$$T_{BA} = \left\langle \Phi^{-}(B,c,d) \middle| V \middle| \Psi^{+}(A,a) \right\rangle, \qquad (4.2)$$

where $\Phi^{-}(B,c,d)$ is the wave function of the final system in the absence of a potential between the outgoing particles *c* and *d*. The exact wave function for the initial state is given by $\Psi^{+}(A,a)$. Both these functions are antisymmetric and the *V* represents the operator carrying information about the proton-proton interaction in the nucleus. If the interaction between *a* and *A* is very weak the entrance wave function $\Psi^{+}(A,a)$ can be replaced by $\Phi^{+}(A,a)$. This makes the amplitude more calculable. Both the wave functions are antisymmetric with respect to interchange of any two nucleons. The operator for the potential of the nucleus (*V*) can also be replaced by a transition operator *t*, and the amplitude becomes

$$T_{BA} = \left\langle \Phi^{-}(B,c,d) \middle| t \middle| \Phi^{+}(A,a) \right\rangle. \qquad (4.3)$$

Because of the impulse approximation the transition operator can be seen as a two body transition operator for free proton-proton scattering (t_{pp}). The wave functions $\Phi^{-}(B,c,d)$ and $\Phi^{+}(A,a)$ can also be broken up into the wave function for each individual particle, giving

$$T_{BA} \approx \left\langle \psi(B)\psi(c)\psi(d)\eta^{-}_{Bcd} \left| t_{pp} \right| \psi(A)\psi(a)\eta^{+}_{Aa} \right\rangle, \qquad (4.4)$$

where η describes the relative motion of the particles and the wave functions ψ are the internal wave functions for various particles. The cross-section and other observables can be calculated by using *equation 4.4* in the PWIA and the DWIA. The PWIA and the DWIA and the results will be evaluated in the following two sections.

4.3 Plane Wave Impulse Approximation

By assuming that there is no interaction between the incoming proton and the target nucleus and the outgoing protons and the residual nucleus, the wave functions (η) can be described by plane wave functions. These functions will be of the form of $e^{\pm i\vec{p}\cdot\vec{r}}$ for the incoming and outgoing channels. The individual nucleon wave functions in *equation 4.4* can then be replaced by asymptotic plane waves neglecting spin. The transition amplitude (*equation 4.4*) thus becomes [Li94]

$$T_{BA} \approx \iint d\vec{r}_c d\vec{r}_d e^{-i\vec{p}_c\cdot\vec{r}_c} e^{-i\vec{p}_d\cdot\vec{r}_d} t_{pp}\left(\left|\vec{r}_c - \vec{r}_d\right|\right) e^{-i\vec{p}_a\cdot\vec{r}_a} \psi_\alpha\left(\vec{r}_d\right), \qquad (4.5)$$

where ψ_α is the nuclear overlap integral which can be written as

$$\psi_\alpha\left(\vec{r}_d\right) = \int d\rho \psi^{*}_{B}(\rho)\psi_A\left(\rho,\vec{r}_d\right). \qquad (4.6)$$

Replacing $\boldsymbol{r} \equiv \boldsymbol{r_c}\text{-}\boldsymbol{r_d}$ in *equation 4.5*, the transition amplitude becomes

$$T_{BA} \approx \int d\vec{r}\, e^{-i\left(\vec{p}_a - \vec{p}_c\right)\vec{r}} t_{pp}\left(\left|\vec{r}\right|\right) \int d\vec{r}_d e^{-i\left(\vec{p}_a - \vec{p}_c - \vec{p}_d\right)\vec{r}_d} \psi_\alpha\left(\vec{r}_d\right). \qquad (4.7)$$

Apply the Born Approximation to the first factor [Mer70]. The result can be expressed as t-matrix element for the proton-proton scattering with respect to the momentum of the particles before and after the scattering.

$$T_{pp} = \left\langle \vec{p}_c, \vec{p}_d \left| t_{pp} \right| \vec{p}_a, -\vec{p}_B \right\rangle. \qquad (4.8)$$

The t_{pp} is the half-off-the-energy-shell amplitude because the proton is bound to the target nucleus.

Applying a Fourier transform to the second factor, the so-called momentum wave function

$$g_\alpha\left(\vec{p_b}\right)=\int d\vec{r_d}e^{-i\vec{d_b}\cdot\vec{r_d}}\psi_\alpha\left(\vec{r_d}\right), \qquad (4.9)$$

is obtained. Thus the transition amplitude becomes

$$T_{BA}\approx T_{pp}.g_\alpha\left(\vec{p_c}\right). \qquad (4.10)$$

Chant *et al.* [Cha77] calculated the differential cross-section as

$$\sigma_{BA}=\frac{2\pi}{\hbar v}|T_{BA}|^2\omega_B. \qquad (4.11)$$

The differential cross-section for the PWIA can then be given by

$$\frac{d^3\sigma}{d\Omega_c d\Omega_d d\Omega E_c}\propto KF.\frac{d\sigma}{d\Omega}\Big|_{pp}.\left|g_\alpha\left(\vec{p_b}\right)\right|^2, \qquad (4.12)$$

where *KF* is a kinematic factor calculated from the kinematic values and $\frac{d\sigma}{d\Omega}\Big|_{pp}$ is a half off-shell p-p cross-section, where

$$\frac{d\sigma}{d\Omega}\Big|_{pp}=|T_{pp}|^2. \qquad (4.13)$$

4.4 Distorted Wave Impulse Approximation

In the DWIA the interaction between the incoming and outgoing protons and the nucleus are taken into account. The interaction between the two outgoing protons and the residual nucleus is also taken into account. Writing the transition amplitude (*equation 4.4*) in the DWIA formalism the wave function for relative motion (η) is replaced by distorted wave functions (γ)

$$T_{BA}\approx\left\langle\psi(B)\psi(c)\psi(d)\gamma^-_{Bcd}\left|t_{pp}\right|\psi(A)\psi(a)\gamma^+_{Aa}\right\rangle. \qquad (4.14)$$

These distorted wave functions can be obtained by solving the Schrödinger equation with a complex optical potential of the Woods-Saxon form. The shape of the radial potential is given by

$$f(r)=\frac{1}{1+e^{\left(\frac{r-R}{a}\right)}}, \qquad (4.15)$$

where $R=r_0M^{\frac{1}{3}}$, is the radius of the nucleus and M is the mass of the nucleus.

According to Jackson *et al.* [Jac65] the Hamiltonian for the initial state can be given by

$$H^{+} = T_{aA} + T_{bB} + V_{aB} + V_{bB} + H_B, \qquad (4.16)$$

where T_{ij} is the relative kinetic operator and V_{ij} is the model potential used to calculate the wave function for the incident and bound protons.

The Hamiltonian for the final state can then be given by

$$H^{-} = T_{cB} + T_{dB} + V_{cB} + V_{dB} + H_B. \qquad (4.17)$$

Solving the Schrödinger equation with the Hamiltonian for the initial state gives

$$\left(T_{aA} + V_{aB} + T_{bB} + V_{bB} + H_B\right)\upsilon^{+} = E_i\upsilon^{+}. \qquad (4.18)$$

But υ^{+} can be written as

$$\upsilon^{+} = \chi_a^{+}\bar{\varphi}\xi, \qquad (4.19)$$

where ξ is the internal wave function of B associated with H_B. To find χ^{+} the following Schrödinger equation for the incoming proton needs to be solved,

$$\left(T_{aA} + V_{aB}\right)\chi_a^{+} = \varepsilon\chi_a^{+}. \qquad (4.20)$$

The bound state wave function ($\bar{\varphi}$) can be found by solving the following equation,

$$\left(T_{bB} + V_{bB}\right)\bar{\varphi} = \bar{\varepsilon}\bar{\varphi}. \qquad (4.21)$$

The distorted wave function for the final state can be written in the same manner, giving

$$\upsilon^{-} = \chi_c^{-*}\chi_d^{-*}\xi. \qquad (4.22)$$

The matrix element (transition amplitude) is taken between the initial and final distorted wave states and becomes

$$T_{if} = \left\langle \upsilon^{-}\middle|V_{ab}\middle|\upsilon^{+}\right\rangle, \qquad (4.23)$$

where V_{ab} is the interaction potential between a and b. If the impulse approximation and the zero-range approximation are applied, the matrix element becomes [Jac65]

$$T_{if} = (2\pi)^{-\frac{3}{2}} t_{pp} \int \chi_c^{-*}\chi_d^{-*}\chi_a^{+}\bar{\varphi}dr, \qquad (4.24)$$

where t_{pp} is the t matrix for free p-p scattering.

By excluding the spin-orbit interaction Chant *et al.* [Cha77] give the final cross-section approximation as the product between a two-body cross-section $\left(\left|\langle t_{pp}\rangle\right|^2\right)$ and a multiplicative factor $\left(\sum_{\Lambda}\left|T_{BA}^{\alpha L\Lambda}\right|^2\right)$

$$\sigma_{BA}^{LJ} = (KF)\times C^2S\times\left|\langle t_{pp}\rangle\right|^2\times\sum_{\Lambda}\left|T_{BA}^{\alpha L\Lambda}\right|^2, \qquad (4.25)$$

where C^2S is the spectroscopic factor, which measures the probability of reaching a specific state by removing a nucleon from the nucleus and $T_{BA}^{\alpha L\Lambda}$ is given by

$$T_{BA}^{\alpha L\Lambda} = \frac{1}{(2L+1)^{\frac{1}{2}}}\int d^3\vec{r}\,\chi_{aB}\left(\vec{r}\right)\chi_{dB}\left(\vec{r}\right)\xi_{L\Lambda}^{\alpha}\left(\vec{r}\right), \qquad (4.26)$$

where the χ's are the incoming and outgoing distorted wave functions and ξ is the single particle wave function of the bound nucleon. This form of cross-section is known as Factorised Distorted Wave Impulse Approximation (FDWIA).

If the spin-orbit terms are included and the incident beam is polarised, the following equation for the differential cross-section was obtained Chant *et al.* [Cha83]

$$\sigma_{BA} = (KF)\times(C^2S)\times\sum_{\rho_c'\rho_d''JM}\frac{\left|\sum_{\rho_a}\langle\rho_c'\rho_d''|T|\rho_a JM\rangle D^{\frac{1}{2}}_{\rho_a\rho_a''}(R_{ap})\right|^2}{(2J+1)}, \qquad (4.27)$$

where

$$\sum_{\rho_a}\langle\rho_c'\rho_d''|T|\rho_a JM\rangle D^{\frac{1}{2}}_{\rho_a\rho_a''}(R_{ap}) = \sum_{\substack{\rho_a\sigma_a\sigma_c\sigma_c'\\ \sigma_d\sigma_d\sigma_{d'}\Lambda}}(2L+1)^{\frac{1}{2}}\langle L\Lambda S_{d'}\sigma_{d'}|JM\rangle\times D^{\frac{1}{2}}_{\rho_a\rho_a''}(R_{ap})\times D^{\frac{1}{2}*}_{\sigma_c\sigma_c'}(R_{ac})$$

$$\times D^{\frac{1}{2}*}_{\sigma_d\sigma_d''}(R_{ad})\times T^{L\Lambda}_{\substack{\sigma_a\sigma_c'\sigma_d''\\ \rho_a\rho_c\rho_d}}\langle\sigma_c\sigma_d|t|\sigma_a\sigma_{d'}\rangle,$$

T is a transition operator,

ρ is a spin projection,

L is the orbital angular momentum quantum number carried by d',

Λ is the projection quantum number,

S_i is a spin quantum number,

σ is the projection quantum number of S_i,

J, M are the total angular momentum quantum number carried by d'',

$D^{\frac{1}{2}}_{\rho_a\rho_a'}(R_{ap})$ is the rotation matrix,

KF is a kinematic factor,

C^2S is the spectroscopic factor,

$\langle\sigma_c\sigma_d|t|\sigma_a\sigma_{d'}\rangle$ is a two-body scattering amplitude,

$T^{L\Lambda}$ is defined by

$$T^{L\Lambda}_{\substack{\sigma_a\sigma_c'\sigma_d'\\ \rho_a\rho_c'\rho_d}} = \frac{1}{(2L+1)^{\frac{1}{2}}}\int \chi^{-*}_{\sigma_c'\rho_c'}(\vec{r'})\chi^{-*}_{\sigma_d'\rho_d'}(\vec{r''})\phi_{L\Lambda}(\vec{r})\chi^{+}_{\sigma_a\rho_a}(\gamma\vec{r})d\vec{r},$$

where $\gamma = \frac{B}{A}$.

4.5 The Computer Program THREEDEE

THREEDEE is a computer program that was written by Chant and Roos [Cha92] to calculate cross-section and polarisation observables in a DWIA for the (p,2p), (p,pn), (n,2n) and (n,pn) reactions. *Equation 4.27* is employed for the calculation of cross-sections.

The program calculates three quantities to obtain the final result. The first is the two-body off-shell scattering amplitude, the second is the bound-state wave function and the third is the distorted wave function describing the incoming and outgoing protons. The calculation of these three quantities is discussed further in this section.

4.5.1 The two-body scattering amplitude

It was shown by Redish *et al.* [Red70] that the (p,2p) knockout reaction is very sensitive to the off-shell behaviour under certain conditions, for example if the energy of the incoming particle is far below ~200 MeV. As the energy of the incoming proton for this experiment was ~200 MeV, the two-body off-shell amplitude can responsibly be approximated by a two-body on-shell amplitude, as is the case with the computer program THREEDEE.

Another approximation that is introduced to make the knockout reaction more calculable is to use the free protons as interacting particles. There are two possible choices for the effective energy at which the on-shell approximation is made. The first is the initial energy

prescription (IEP). In this prescription, the effective energy is calculated by taking the energy of the incoming particle and the mass of the target proton. The effective two-body relativistic energy (E_{rel}), is calculated with the following equation [Are97]

$$E_{rel} = E_a + \sqrt{P_b^2 + M_b^2}\,, \qquad (4.28)$$

where E is the energy, P the momentum and M the rest mass of the particles as indicated.
In the final energy prescription (FEP), the properties of the outgoing particles are used to calculate the E_{rel}, as stated in the following equation [Are97]

$$E_{rel} = \sqrt{M_c^2 + M_d^2 + 2E_cE_d - 2P_cP_d\cos\theta}\,, \qquad (4.29)$$

with the variables the same as in the previous equation and θ the angle between the two outgoing particles. Of these two prescriptions, the FEP is the most commonly used [Are97] and all the results of the theoretical calculation were done with the FEP after checking that the results of the two prescriptions differ negligibly.

4.5.2 The bound state wave function

The general form of the potential used to determine bound-state wave function consists of a central potential term, a spin orbit term and a Coulomb potential term [Cha92]

$$-U(r) = \frac{V_c}{1+e^x} + g\left(\vec{l}\cdot\vec{\sigma}\right)\frac{1}{r.a_{so}}\cdot\frac{V_{so}e^{xs}}{\left(1+e^{xs}\right)^2} - U_{coul}(r), \qquad (4.30)$$

where

$$x = \frac{r - R_cM^{1/3}}{a_c}$$

and

$$xs = \frac{r - R_{so}M^{1/3}}{a_{so}},$$

where $U_{coul}(r)$ is the Coulomb potential due to a spherical charge of radius $R_{coul}M^{1/3}$

V_c is the strength of the central potential,

V_{so} is the strength of the spin-orbit potential,

R_c the radius of the central potential,

R_{so} the radius of the spin-orbit potential,

a_c the diffuseness parameter of the central potential,

a_{so} the diffuseness parameter of the spin-orbit potential,

$\vec{l}$ is the orbital angular momentum,

$\vec{\sigma}$ is the intrinsic spin and

M is the mass of the recoil nucleus (in atomic mass units).

Furthermore

$$\vec{l}\cdot\vec{\sigma} = l \quad \text{for } j = l + s$$

or

$$\vec{l}\cdot\vec{\sigma} = -l - 1 \quad \text{for } j = l - s. \qquad (4.31)$$

Two different parameter sets were used for this potential to calculate the bound-state wave function. In the first set the spin-orbit part of the Woods-Saxon potential is optimised, using experimental results [Dud81]. In the second set the depth and radius of the Woods-Saxon potential are extrapolated from positive to negative energies by using an iteration procedure [Are97, Mah88]. These two sets are listed in *Table 4.A.*

Table 4.A: The bound-state parameters that were used.

	Set 1 [Dud81]	*Set 2* [Are97, Mah88]
R_{coul}	1.275 fm	1.250 fm
R_c	1.275 fm	1.198 fm
R_{so}	1.300 fm	1.198 fm
a_c	0.700 fm	0.700 fm
a_{so}	0.700 fm	0.700 fm
V_c	58.62 MeV	⊗
V_{so}	11.685 MeV	5.00 MeV

4.5.3 The distorted wave functions

Distorted wave functions are obtained by solving the Schrödinger equation with a complex optical potential. The equation for the central optical potential that Chant *et al.* uses in THREEDEE is

⊗ Potential depth varied to reproduce separation energy.

$$-U(r)_{central} = \frac{V}{1+e^{x}} + \frac{iW}{1+e^{x'}} + \frac{4iW_d e^{x'}}{\left(1+e^{x'}\right)^2} - U_{coul}(r), \qquad (4.32)$$

where

$$x = \frac{r - r_o M^{1/3}}{a}$$

and

$$x' = \frac{r - r_o' M^{1/3}}{a'},$$

where V is the strength of the real part of the central potential,

W is the strength of the imaginary part of the central potential,

W_d is the strength of the surface absorptive part of the potential,

M is the mass of the target nucleus (in atomic mass units),

$U_{coul}(r)$ is the Coulomb potential due to a spherical charge of radius $R_{coul} M^{\frac{1}{3}}$,

r_0 is the real central radius parameter,

r_0' is the imaginary central radius parameter,

a is the real central diffuseness parameter and

a' is the imaginary central diffuseness parameter.

This central potential includes a Coulomb term and a complex central potential term. To generate the distorted wave functions for the incident and outgoing particles, the spin-orbit interaction and the exchange interaction need to be incorporated. The total potential, for calculating the distorted wave functions, includes these terms and is given by

$$-U(r) = -U(r)_{central} + g\left(\vec{l}\cdot\vec{\sigma}\right)\frac{1}{r a_{so}} \cdot \frac{\left(V_{so} + iW_{so}\right)e^{x_s}}{\left(1+e^{x_s}\right)^2} + (-1)^l \frac{V_{ex}}{1+e^{x_{ex}}}, \qquad (4.33)$$

where

$$x_s = \frac{r - r_{so} M^{1/3}}{a_{so}}$$

and

$$x_{ex} = \frac{r - r_{ex} M^{1/3}}{a_{ex}},$$

where V_{so} is the strength of the real part of the spin-orbit potential,

W_{so} is the strength of the imaginary part of the spin-orbit potential,
V_{ex} is the strength of exchange potential,
r_{so} is the radius parameter of the spin-orbit potential,
r_{ex} is the radius parameter of the exchange part of the potential,
a_{so} is the spin-orbit diffuseness parameter and
a_{ex} is the diffuseness parameter of the exchange part of the potential,
and l is the parity.

Three different parameter sets were used, for the optical potentials, to calculate the cross-sections and analysing powers. Nadasen *et al.* [Nad81], Schwandt *et al.* [Sch82] and Madland [Mad87] determined these sets of parameters.

Nadasen *et al.* used relativistic kinematics and a relativistic extension of the Schrödinger equation. The phenomenological form of the optical potential parameters were obtained from the experimental cross-sections for elastic scattering of protons from ^{40}Ca, ^{90}Zr and ^{208}Pb. This was done over the energy range 80-180 MeV.

The parameter set of Schwandt *et al.* was extracted from data on the same target, as those of Nadasen *et al.* but in addition to cross sections, experimental analysing power were also available. The parameter set of Madland is an adjustment of that of Schwandt *at al.* to resolve a problem with the reaction cross section predicted by the set for incident energies above 200 MeV. All the optical potential parameters are listed in *Table 4.B, Table 4.C* and *Table 4.D*. A and z in the table, are the mass and charge, respectively of the target nuclei and γ is a relativistic kinematic factor given by the following equation

$$\gamma = 1 + \frac{E}{mc^2}, \qquad (4.34)$$

where E is the kinetic energy and m the rest mass of the incoming proton.

Table 4.B: Optical model potential parameter set of Nadasen.

V	$\gamma \cdot \{92.5 \cdot (1 - 0.155 \cdot \mathrm{Ln\,E}) + 25 \cdot (1 - 2z/\mathrm{M})\}$
W	$\gamma \cdot 7.4$
r_0	1.21
r_0'	1.37 + 3.5/M
a	0.77
a'	$0.36 + 0.036 \cdot \mathrm{M}^{\frac{1}{3}}$
$\mathrm{V_{so}}$	$\gamma \cdot 15 \cdot (1 - 0.16 \cdot \mathrm{Ln\,E})$
$\mathrm{W_{so}}$	$-1.2 \cdot \gamma$
r_{so}	$0.985 + 0.0002 \cdot \mathrm{M} + 0.00064 \cdot \mathrm{E}$
a_{so}	$0.52 + 0.00086 \cdot \mathrm{M}$
$\mathrm{W_d}$	0.0
$\mathrm{V_{ex}}$	0.0
r_{ex}	1.0
a_{ex}	1.0
$\mathrm{R_{coul}}$	1.25

Table 4.C: Optical model potential parameter set of Schwandt.

V	$\gamma \cdot \{105.5 \cdot (1 - 0.1625 \cdot \mathrm{Ln\,E}) + 16.5 \cdot (1 - 2z/M)\}$
W	$\gamma \cdot \{6.6 + 2.73 \times 10^{-2} \cdot (E - 80) + 3.87 \times 10^{-6} \cdot (E - 80)^3\}$
r_0	$\begin{cases} 1.125 + 1.0 \times 10^{-3} \cdot E \Rightarrow E \leq 130\ \mathrm{MeV} \\ 1.255 \Rightarrow E > 130\ \mathrm{MeV} \end{cases}$
r_0'	$1.65 - 2.4 \times 10^{-3} \cdot E$
a	$0.675 + 3.1 \times 10^{-4} \cdot E$
a'	$0.32 + 2.5 \times 10^{-3} \cdot E$
V_{so}	$\gamma \cdot \{19.0 \cdot (1 - 0.166 \cdot \mathrm{Ln\,E}) - 3.75 \cdot (1 - 2z/M)\}$
W_{so}	$\gamma \cdot \{7.5 \cdot (1 - 0.248 \cdot \mathrm{Ln\,E})\}$
r_{so}	$0.920 + 0.0305 \cdot M^{\frac{1}{3}}$
a_{so}	$\begin{cases} 0.768 - 0.0012 \cdot E \Rightarrow E \leq 140\ \mathrm{MeV} \\ 0.60 \Rightarrow E > 140\ \mathrm{MeV} \end{cases}$
W_d	0.0
V_{ex}	0.0
r_{ex}	1.0
a_{ex}	1.0
R_{coul}	1.25

Table 4.D: Optical model potential parameter set of Madland.

V	$\gamma \cdot \{1055 \cdot (1 - 0.1625 \cdot \text{Ln E}) + 16.5 \cdot (1 - 2z/M)\}$
W	$\begin{cases} \gamma \cdot \{6.6 + 2.73\times10^{-2} \cdot (E - 80) + 3.87\times10^{-6} \cdot (E - 80)^3\} \Rightarrow E \le 140 \text{ MeV} \\ \gamma \cdot \{7.314 + 0.0462 \cdot E\} \Rightarrow E > 140 \text{ MeV} \end{cases}$
r_0	$\begin{cases} 1.125 + 1.0\times10^{-3} \cdot E \Rightarrow E \le 130 \text{ MeV} \\ 1.255 \Rightarrow E > 130 \text{ MeV} \end{cases}$
r_0'	$\begin{cases} 1.65 - 2.4\times10^{-3} \cdot E \Rightarrow E \le 140 \text{ MeV} \\ 1.17 \Rightarrow E > 140 \text{ MeV} \end{cases}$
a	$0.675 + 3.1\times10^{-4} \cdot E$
a'	$\begin{cases} 0.27 + 2.5\times10^{-3} \cdot E \Rightarrow E \le 140 \text{ MeV} \\ 0.79 \Rightarrow E > 140 \text{ MeV} \end{cases}$
V_{so}	$\gamma \cdot \{19.0 \cdot (1 - 0.166 \cdot \text{Ln E}) - 3.75 \cdot (1 - 2z/M)\}$
W_{so}	$\gamma \cdot \{7.5 \cdot (1 - 0.248 \cdot \text{Ln E})\}$
r_{so}	$0.920 + 0.0305 \cdot M^{\frac{1}{3}}$
a_{so}	$\begin{cases} 0.768 - 0.0012 \cdot E \Rightarrow E \le 140 \text{ MeV} \\ 0.60 \Rightarrow E > 140 \text{ MeV} \end{cases}$
W_d	0.0
V_{ex}	0.0
r_{ex}	1.0
a_{ex}	1.0
R_{coul}	1.25

4.6 Calculation of the Spectroscopic Factor

As it was shown in Chapter 3 it was not possible to resolve all four of the energy states. Two energy peaks could however, be resolved. The first one incorporating the ground state and the first exited state ($3s_{1/2}$,$2d_{3/2}$) and the second one incorporating the two higher states ($1h_{11/2}$,$2d_{5/2}$). The cross-sections were therefore calculated for these two peaks, as well as for all four the states combined. For the combination of all these states, the relative spectroscopic factors obtained by Royer *et al.* [Roy70] were used. These values are tabled in *table 4.E.*

Table 4.E: The relative spectroscopic factors as obtained by Royer et al.

States	*Relative Spectroscopic Factors*
$3s_{1/2}$	3.9
$2d_{3/2}$	7.4
$2d_{5/2}$	7.2
$1h_{11/2}$	15.6

A normalisation method was used to fit the theoretical cross-section to the experimental cross-section. This was achieved with a chi-square fit, where by χ^2 was minimised [Leo94]

$$\chi^2 = \sum_i \left(\frac{x_i - c\mu_i}{\sigma_i} \right)^2 , \qquad (4.35)$$

where x_i is the experimental cross-section,

μ_i is the theoretical cross-section,

σ_i is the statistical error associated with the experimental cross-section and

c is the normalisation constant.

These normalisation values that were obtained, were taken as the spectroscopic factors.

Chapter 5: RESULTS

5.1 Introduction

In this chapter, the results of the experiment are given and some of the factors influencing the theoretical calculation are discussed. In the second section, the comparisons between the theoretical and experimental results for the differential cross-section are discussed. The next section discusses the spectroscopic factors that were extracted. A comparison between the theoretical and experimental results for the analysing power is then discussed. In these paragraphs reference is made to the optical model potential, bound state and the role of valence states.

5.2 Differential Cross-section Energy Distributions

As was mentioned before, in this work the two resolved knock-out peaks each contain two unresolved states. The larger peak (see *figure 3.6*) contains the ground state and the first excited energy state, that is $3s_{1/2}$ and $2d_{3/2}$, and the smaller left peak contained the two more deeply-bound states, viz. $1h_{11/2}$ and $2d_{5/2}$.

The experimental and theoretical cross-section of all four states together ($3s_{1/2}$,$2d_{3/2}$,$1h_{11/2}$,$2d_{5/2}$), from here on referred to as the summed states, are plotted in *figure 5.1*. The cross-section is also plotted for each of the two resolved peaks each containing two states, namely the $3s_{1/2}$ and $2d_{3/2}$, from here on referred to as the sd-state, and the combination of $1h_{11/2}$ and $2d_{5/2}$ referred to as the hd-state. These plots are shown in *figures 5.2* and *figures 5.3* respectively. The relative contribution of the theoretical calculations for each state toward the final theoretical value, for all the combinations is illustrated in *figure 5.4*. In the graph of the sd-state, the dominance of the $3s_{1/2}$ state in the region of 145 MeV is clearly evident. For the hd-state, the $2d_{5/2}$ state dominates the

combination (see *figure 5.4*). Thus any information that is extracted from this combination (see *figure 5.3*) can be attributed as mostly due to the $2d_{5/2}$ state.

5.2.1 Sensitivity of the choice of the optical model potential

To investigate the sensitivity of the theoretical cross section to the choice of the optical model potential the values were calculated using three different optical model potentials of the Woods-Saxon form. The parameters used were those of Nadasen *et al.* [Nad81] (in *figure 5.1* to *figures 5.3* marked as *A*), Schwandt *et al.* [Sch82] (in *figure 5.1* to *figures 5.3* marked as *B*) and Madland [Mad87] (in *figure 5.1* to *figures 5.3* marked as *C*). The statistical errors of the experimental data are shown in the figures.

The three optical model potentials that were used, were non-relativistic and of the Wood-Saxon form. All the calculated results for the three optical model potentials compare well with the experimental cross-section energy distributions (see *figure 5.1* to *figures 5.3*). Therefore the specific choice of parameter set does not influence the predicted energy distribution for the ^{208}Pb(p,2p)^{207}Tl reaction.

5.2.2 Sensitivity of the choice of the bound state

The three calculations shown in *figures 5.1* to *figures 5.3* all used the same bound state parameters given by Arendse [Are97, Mah88]. In addition the calculation with the Nadasen optical model potentials was also done with a different bound state, given by Dudek *et al.* [Dud81]. It should be noted, as mentioned before, that the two sets of bound state parameters were obtained in very different ways. The first set of bound state parameters were extracted in a procedure for which the spin-orbit part of the Woods-Saxon bound state potential is optimised, using experimental results [Dud81]. For the second set, the depth and radius of the Woods-Saxon potential are extrapolated from positive to negative energies by using an iteration procedure [Are97, Mah88].

Because the Nadasen potential was used successfully in other studies to predict the experimental data [Cha83, Cow91] this set was chosen for the investigation of the influence of the choice of bound state parameters. The selection of the Nadasen potential, was

however, an arbitrary choice, as all three different potentials give, within 5%, the same results. The shape of the calculated distributions for these two bound states does not differ significantly as can seen. As can be seen in *figure 5.5.*

5.3 The Spectroscopic Factor

The experimental spectroscopic factor of a state is extracted by normalising the theoretical energy distribution to the experimental values. The uncertainty on the extracted spectroscopic factor is due to a combination of the uncertainty of various quantities that enter into the calculation of the theoretical cross-sections. These contributions to the uncertainty are listed in *table 5.A* and the total error in the theoretical calculations was obtained by quadratic summation of these values.

Table 5.A: Errors in the theoretical calculations[Are97].

Sources of uncertainty	*Uncertainty (%)*
Uncertainty due to optical model potential	12
Uncertainty due to the bound state parameters	15
Uncertainty due to summation factors	16
Total Error in the theoretical calculations	**25**

The quadratic summation of the systematic errors (*table 3.D*) and the errors on the theoretical calculations (*table 5.A*) determine the total error in the spectroscopic factors. The total error on the spectroscopic factors amount to **27%**.

The final extracted spectroscopic factors (with the errors) for the different optical potentials and bound states were extracted and are listed in *table 5.B* and *table 5.C*.

Table 5.B: The extracted spectroscopic factors for the different optical potentials with the bound state given by Arendse [Are97, Mah88].

States	*Nadasen et al. [Nad81]*	*Schwandt et al. [Sch82]*	*Madland [Mad87]*
all states	0.70 ± 0.19	0.87 ± 0.23	0.86 ± 0.23
sd-state	0.63 ± 0.17	0.82 ± 0.22	0.81 ± 0.22
hd-state	0.54 ± 0.15	0.61 ± 0.16	0.60 ± 0.16

Table 5.C: The extracted spectroscopic factors with the bound state given by Dudek et al. [Dud81] and the optical potential of Nadasen et al. [Nad81].

States	*Nadasen et al. [Nad81]*
all states	0.46 ± 0.12
sd-state	0.43 ± 0.12
hd-state	0.33 ± 0.09

Table 5.D: Spectroscopic factors from other studies.

Study	*Spectroscopic factors for the* $3s_{1/2}$ *state*
Neveling [Nev98]	0.73 ± 0.19
Arendse [Are97]	0.7 to 0.8
Udías *et al.* [Udí93]	0.65 to 0.73
Jin *et al.* [Jin92]	0.71
McDermott [McD90]	0.65

The spectroscopic factors for the combination of the sd-states and hd-states and the combinations of all the states were extracted for the three different potentials. These spectroscopic factors, for the different potentials, are in reasonable agreement. The Nadasen potential was used with two different bound states and compared in *tables 5.B* and *tables 5.C* it suggests that the choice of a bound state has a significant effect on the spectroscopic factors. The shapes of the calculated differential cross-sections, using the two different bound state parameters, however compares well (see *figure 5.4*). Nevertheless, the difference is within error margins.

It should be noticed that the extracted spectroscopic factor using the bound state given by Arendse [Are97, Mah88], gave a value of **0.70 ± 0.19** for the combined states, which compares very well with the values that were found in other studies (see *table 5.D).* On the other hand the bound state given by Dudek *et al.* [Dud81] gave a spectroscopic factor of **0.46 ± 0.12**, which, although somewhat low, is still reasonably consistent with the result from previous studies (see *table 5.D).*

5.4 Analysing Power

The analysing power of all four states together ($3s_{1/2}$,$2d_{3/2}$,$1h_{11/2}$,$2d_{5/2}$), referred to as all the states, is plotted in *figure 5.6*. The analysing power is also plotted for the sd-state and the the hd-state. These plots are shown in *figures 5.7* and *figures 5.8* respectively.

As previously, for the cross-section energy distributions, the theoretical distributions were calculated using three different optical model distorting potentials of the Woods-Saxon form, but using the same bound state parameters as given by Arendse [Are97, Mah88]. These potentials were those of Nadasen *et al.* [Nad81] (in *figure 5.6* to *figures 5.8* marked as *A*), Schwandt *et al.* [Sch82] (in *figure 5.6* to *figures 5.8* marked as *B*) and Madland [Mad87] (in *figure 5.6* to *figures 5.8* marked as *C*). The error bars on the experimental data show the statistical errors.

In addition, the calculations with the Nadasen optical model potentials were also done with the bound state of Dudek *et al.* [Dud81]. No improvement in the agreement between the theoretical calculations and experimental data is obtained with the alternative bound state parameter set. The comparison between the analysing powers predicted by the hd-state for the two sets of bound state parameters is shown in *figure 5.9.*

The theoretical calculations for the combination of the two valence states $1h_{11/2}$ and $2d_{5/2}$ gave a reasonable agreement with the experimental values (see *figure 5.8*). The theoretical calculations for the other valence states did not agree with the experimental data.

Figure 5.10 shows the theoretical calculations using the three optical models potentials for the hd-state combination. Of course, of the three optical model potentials, the Nadasen potential gave results which compare best with the experimental data for analysing power of the hd-state, as is evident from *figure 5.8*

5.5 Summary of Results

The theoretical cross-section calculations predict the experimental cross-section data well for all combinations of distortions, potentials and bound states, both with regard to the shape of the energy distributions, as well as the absolute magnitude of the spectroscopic factor.

The theoretical analysing power values did not agree with the experimental analysing power data. The only exception is for the hd-state, which is described reasonably well by the distorting potential parameters of Nadasen.

The extracted spectroscopic factors are consistent with the result obtained in previous studies done by Arendse [Are97] and Neveling [Nev98].

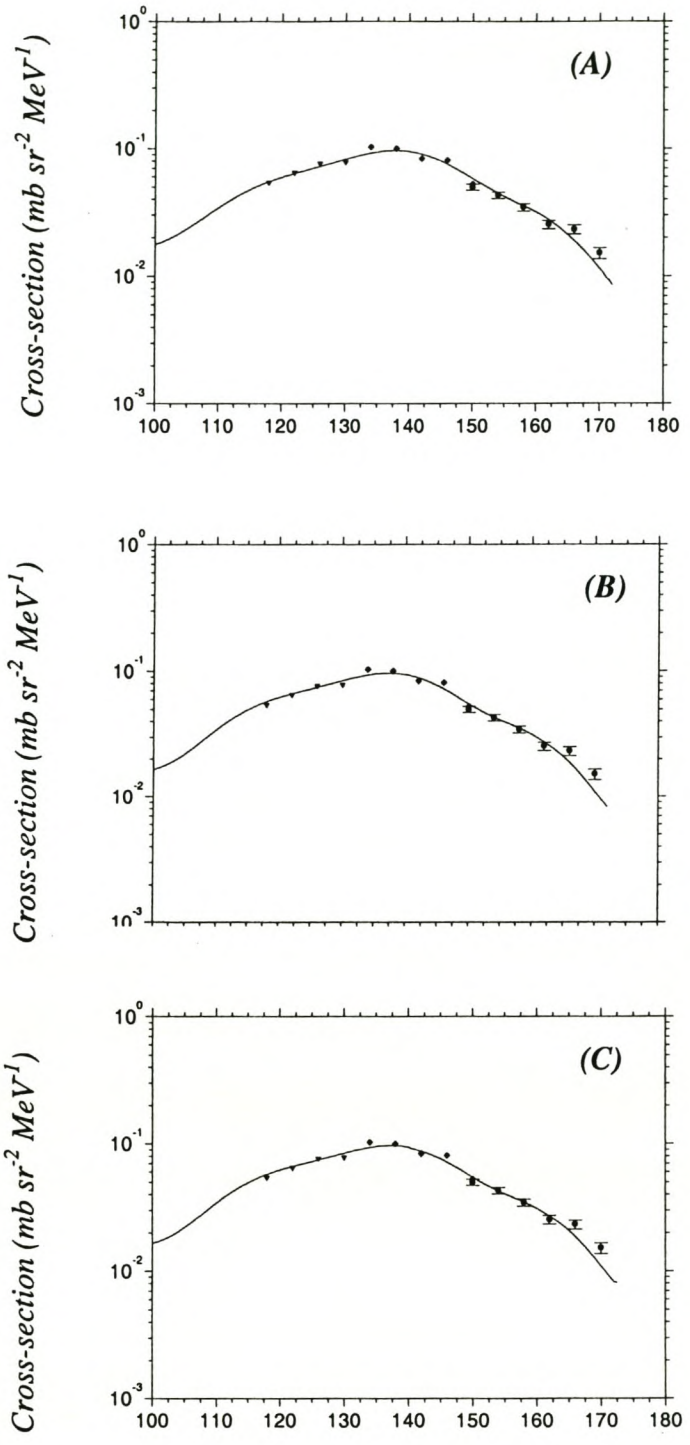

Figure 5.1: The cross-section as a function of the proton energy for the sum of all four states using the Nadasen [Nad81], Schwandt [Sch82] and Madland [Mad87] potentials for the theoretical calculations. The results are plotted as a function of the energy of the proton observed in the K600 detector at an angle of 28° for a secondary angle at 54.6° on opposite sides of the incident beam.

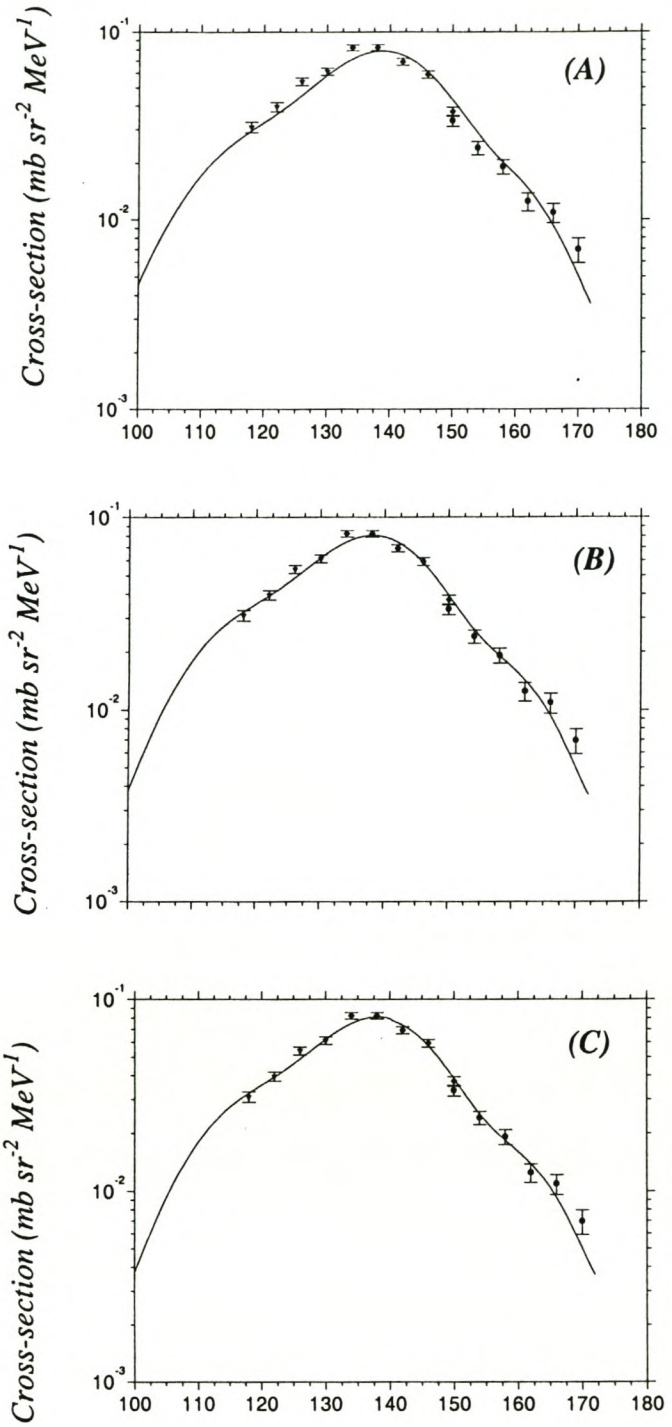

Figure 5.2: The cross-section as a function of the proton energy for the sum of the sd-states using the Nadasen [Nad81], Schwandt [Sch82] and Madland [Mad87] potentials for the theoretical calculations. Also see the caption to Figure 5.1.

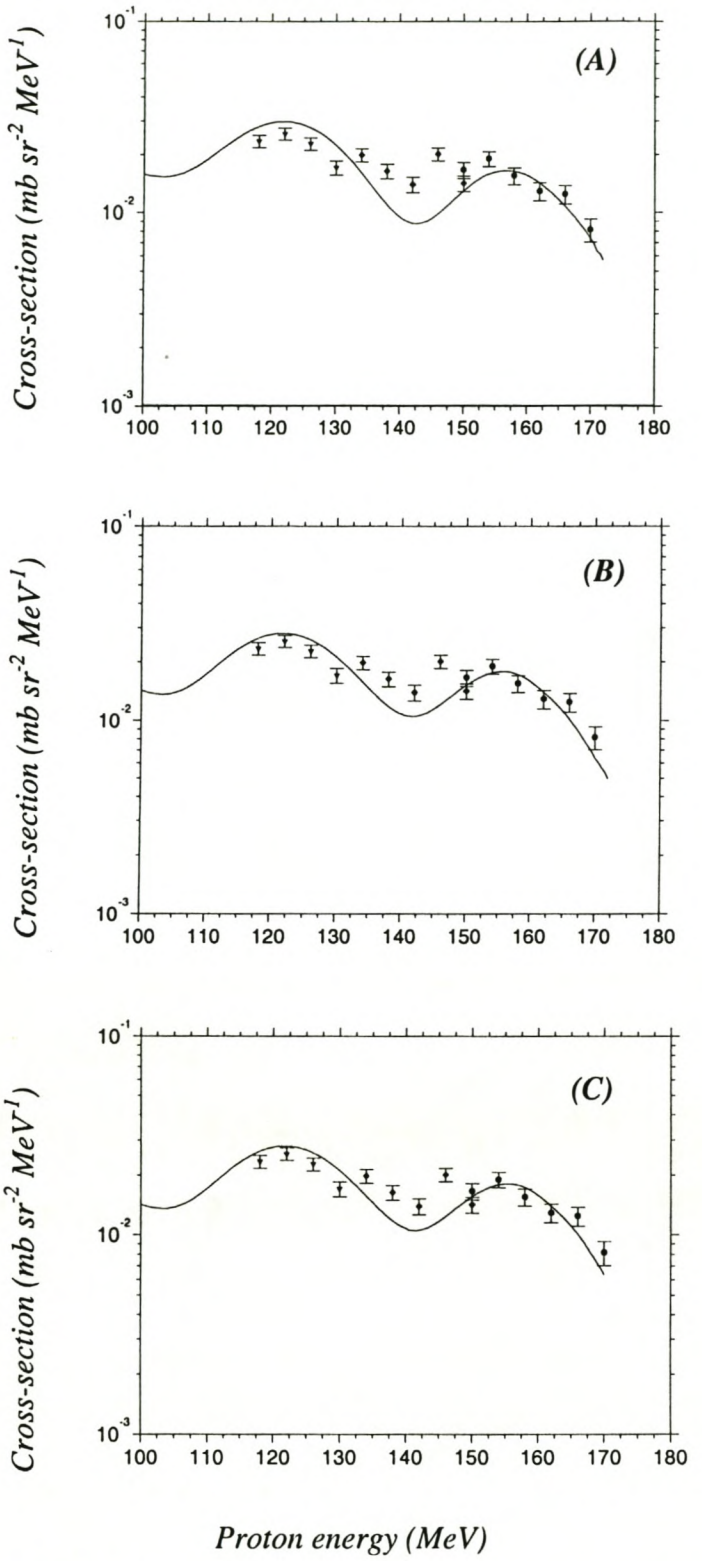

Figure 5.3: The cross-section as a function of the proton energy of the hd-states using the Nadasen [Nad81], Schwandt [Sch82] and Madland [Mad87] potentials for the theoretical calculations. Also see the caption to figure 5.1.

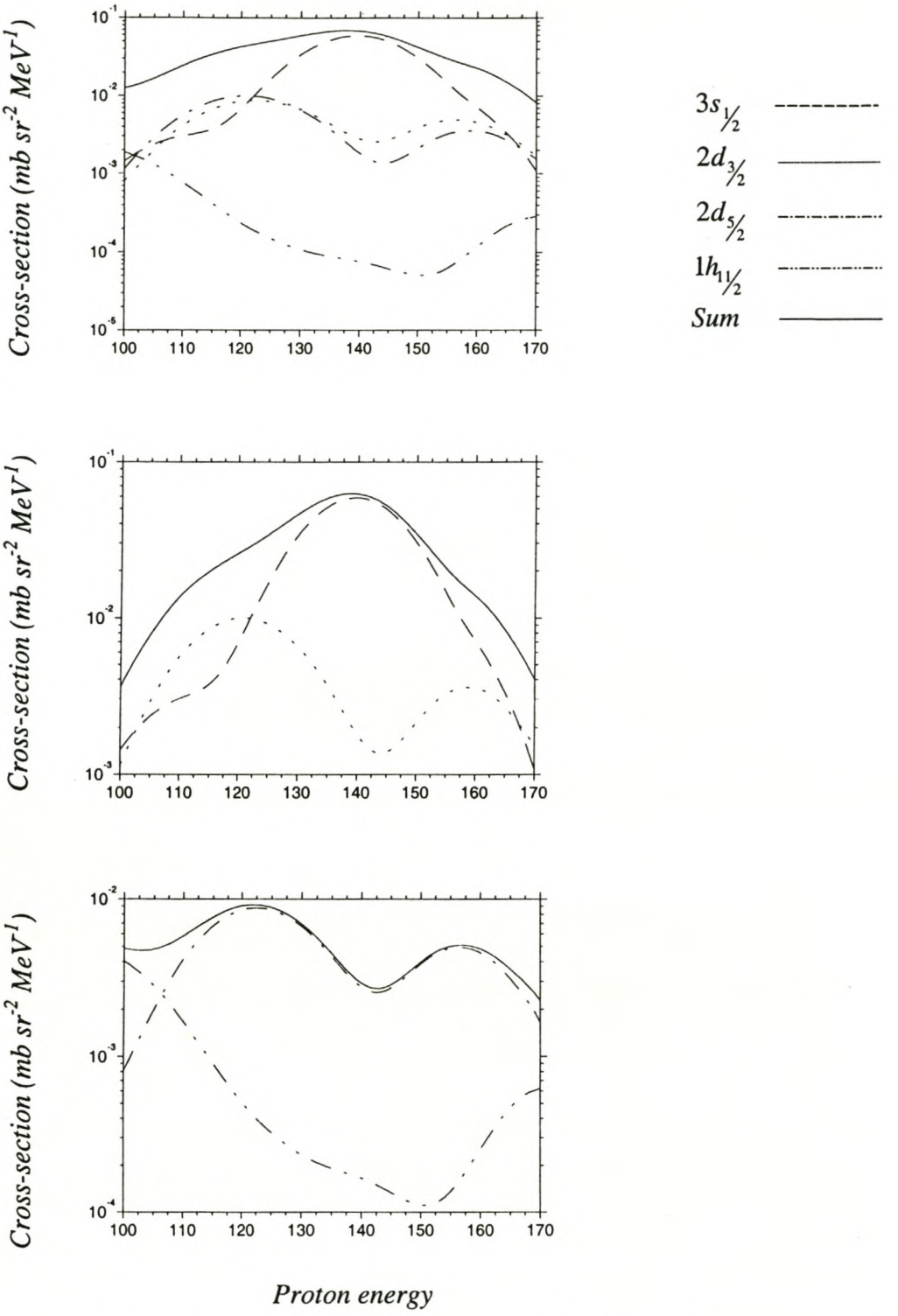

Figure 5.4: The theoretical cross-section for the different valence states, as well as the summed cross-section for the combinations using the Nadasen [Nad81] potential and the Arendse bound state [Are97].

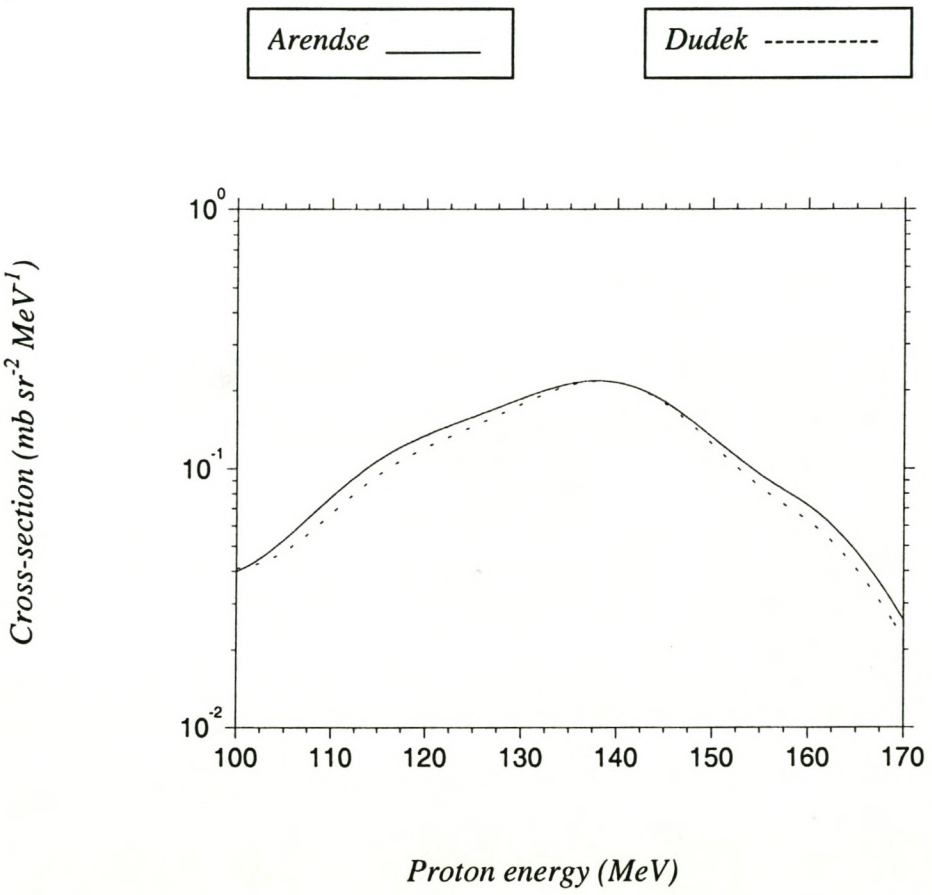

Figure 5.5: The cross-section as a function of the proton energy using Dudek et al. [Dud81] and Arendse [Are97, Mah88] bound states for the theoretical calculations. The two sets have been normalised at an energy of 140 MeV.

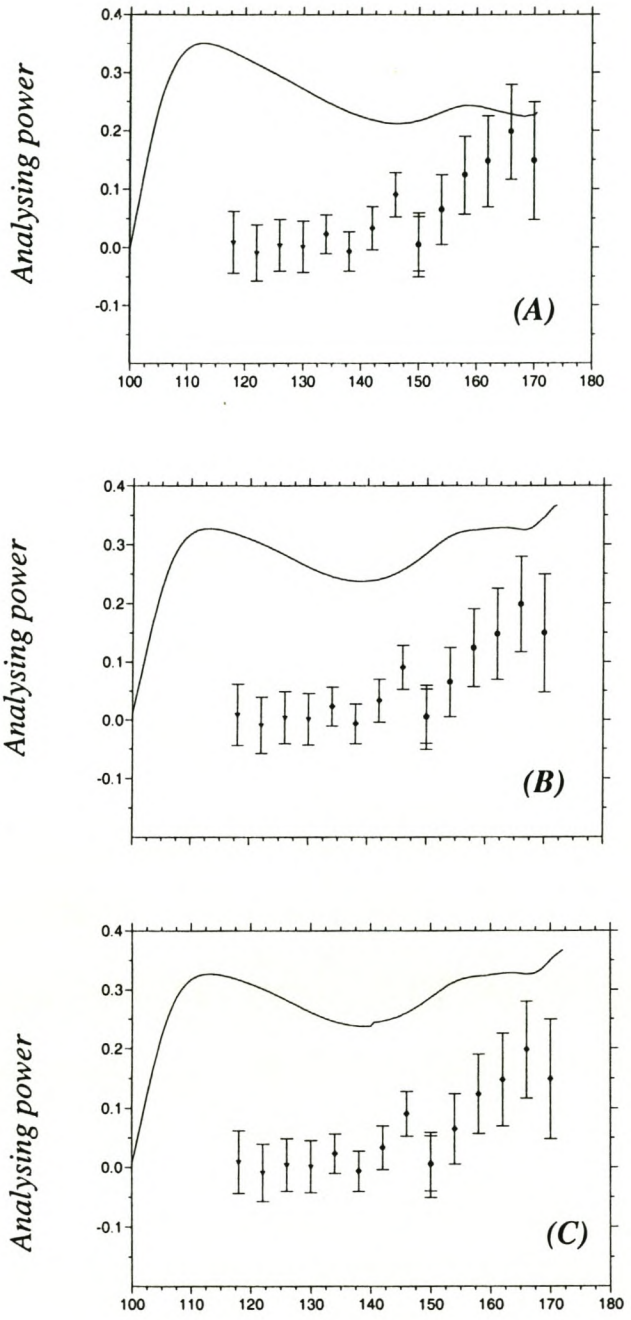

Figure 5.6: The analysing power as a function of the proton energy using the Nadasen [Nad81], Schwandt [Sch82] and Madland [Mad87] potentials for the theoretical calculations for the sum of all four states.

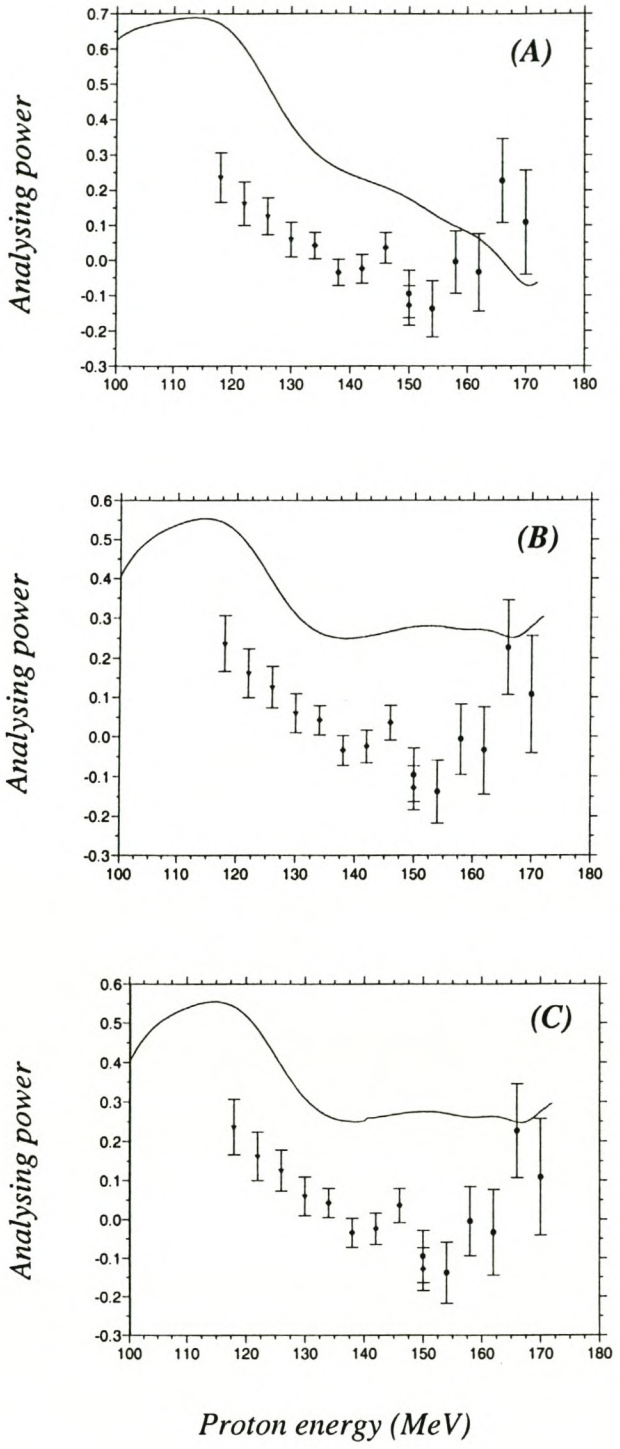

Figure 5.7: The analysing power as a function of the proton energy for the sd-states using the Nadasen [Nad81], Schwandt [Sch82] and Madland [Mad87] potentials for the theoretical calculations.

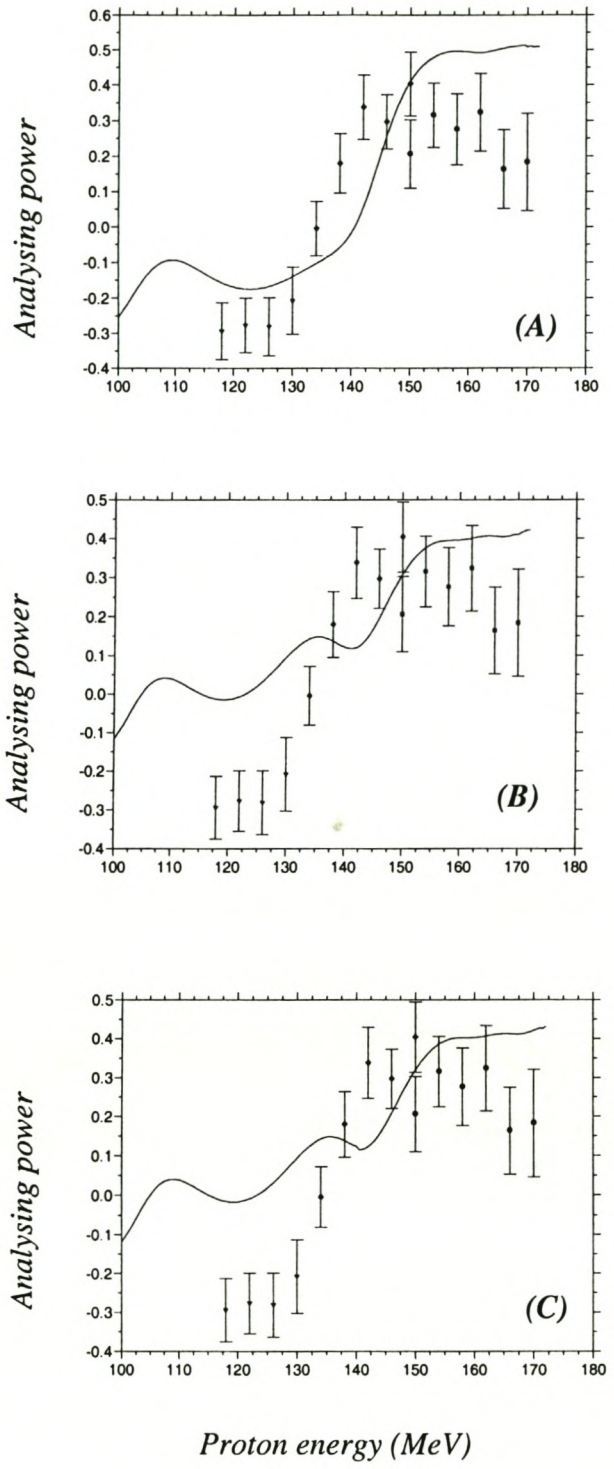

Figure 5.8: The analysing power as a function of the proton energy for the hd-states using the Nadasen [Nad81], Schwandt [Sch82] and Madland [Mad87] potentials for the theoretical calculations.

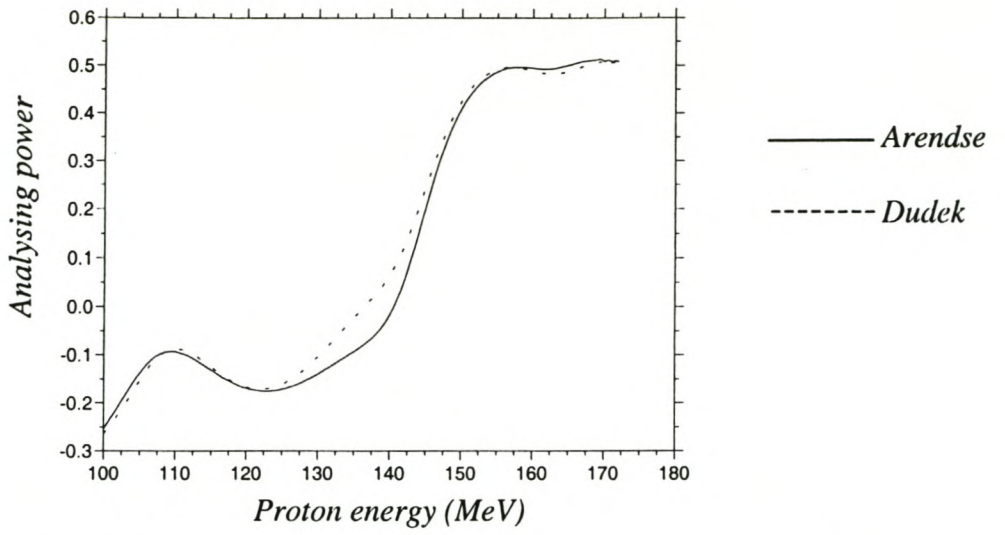

Figure 5.9: The analysing power as a function of the proton energy for Nadasen potential [Nad81] using the Arendse [Are97] and the Dudek [Dud81] bound-states.

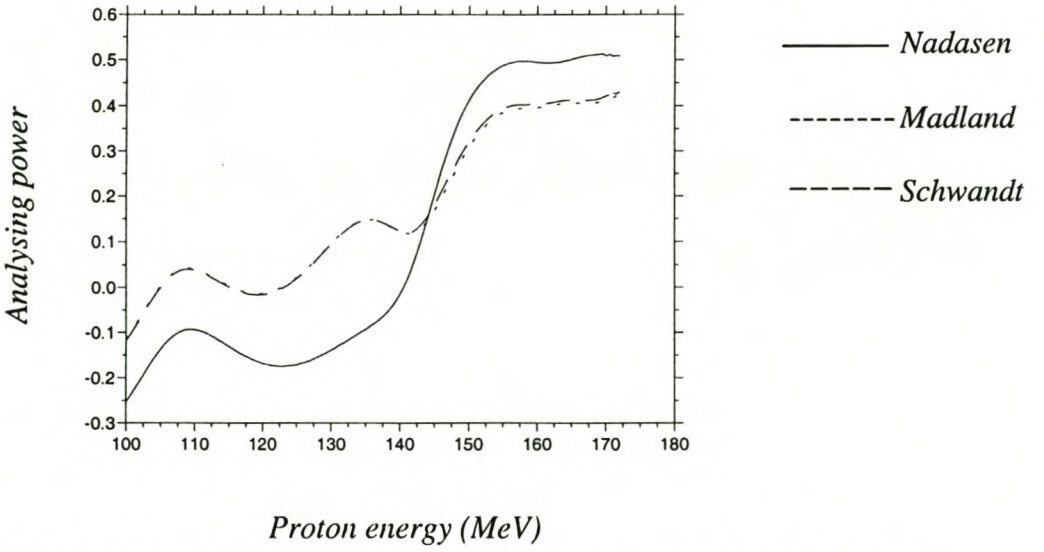

Figure 5.10: The analysing power as a function of the proton energy using Nadasen potential [Nad81], Madland potential [Mad87] and Schwandt potential [Sch82] for the theoretical calculations.

Chapter 6: SUMMARY AND CONCLUSION

In this work the $^{208}Pb(p,2p)^{207}Tl$ quasi-free scattering process was investigated at a coplanar angle pair of 54.6° and 28° on opposite sides of the incident beam. The experimental data were obtained at the National Accelerator Centre (NAC) using incident protons of 200 MeV, which were accelerated by a separated sector cyclotron. The two outgoing particles, from the knock-out reaction, were detected in coincidence and their energies were measured using a K600 magnetic spectrometer and a ΔE-E silicon/germanium telescope detector.

The experimental cross section and analysing power distributions were compared with theoretical quantities for the Distorted Wave Impulse Approximation (DWIA). Spectroscopic factors were also extracted. It was found that the theoretical cross-sections predict the experimental cross-section data well for all combinations of distorting potentials and bound state parameters. This was true with regard to the shape of the energy distributions, as well as the absolute magnitude of the spectroscopic factor. This agreement is consistent with the results obtained in earlier studies. Consequently this finding inspired confidence in the accuracy of the data that were measured, and by implication, the validity of the experimental techniques that were exploited in this work.

The theoretical analysing power distributions, however, did not agree with the experimental analysing power data. One should keep in mind that the four energy states could not be fully resolved, but only in pairs of two viz. $3s_{1/2}$ with $2d_{3/2}$ and $1h_{11/2}$ with $2d_{5/2}$. Therefore it is not possible to explore this phenomenon further with the present data. It would provide insight if it could be determined whether the problem is common to the analysing power distributions of all four individual states.

Future work could be directed towards either software deconvolution to separate the data for the four states, or to improving the inherent energy resolution further. The latter aim, of course, would require an understanding of the deterioration of the energy resolution in the present experiment to a value that is twice as high as that contributed by only the detectors.

We speculate that poor energy resolution is caused to an appreciable extent by beam quality or kinematic spread.

In conclusion, the results obtained for the spectroscopic factors and cross sections suggest that the DWIA provides a reasonable model of the main features of the knockout processes. More subtle aspects that determine features of the analysing power distributions are clearly not understood.

REFERENCES

[Are97] Nuclear distortions in the (p,2p) knockout reaction on ^{208}Pb at an incident energy of 200 MeV
G.J. Arendse
Ph.D. thesis (1997)
University of Stellenbosch

[Cha77] Distorted-wave impulse-approximation calculations for quasifree cluster knockout reactions
N.S. Chant and R.G. Roos
Physical Review C15 (1977) 57

[Cha83] Spin-orbit effects in quasifree knockout reactions
N.S. Chant and R.G. Roos
Physical Review C27 (1983) 1060

[Cha92] THREEDEE code
N.S. Chant
University of Maryland (1992) (Unpublished)

[Cow91] Quasifree knockout in ^{16}O(p,2p)^{15}N at an incident energy of 151 MeV
A.A. Cowley, J.J. Lawrie, G.C. Hillhouse, D.M Whittal, S.V. Förtsch, J.V. Pilcher, F.D. Smit and P.G. Roos
Physical Review C44 (1991) 329

[Cow95] Distortion in proton-knockout reactions.
A.A. Cowley, G.J. Arendse, J.A. Stander and W.A. Richter
Physics Letters B359 (1995) 300

[Dud81] Woods-Saxon potential parameters optimized to the high spin spectra in the lead region
J. Dudek, Z. Szymanski and T. Werner
Physical Review C23 (1981) 920

[For92] Proton emission in pre-equilibrium reactions induced by incident protons of 100 and 200 MeV
S.V. Förtsch
Ph.D. thesis (1992)
University of Pretoria

[Fra91] Subatomic Physics
H. Frauenfelder and E.M. Henley
Prentice Hall (1991)

[Gib71] Nuclear reactions
W.M. Gibson
Penguin Books (1971)

[Hae74] Polarization experiments; Polarized Beams,
edited by J. Cerny (California 1974), p151
W. Haeberli
Nuclear spectroscopy and reactions (Part A)

[Ham90] Global Dirac optical potential for elastic scattering from heavy nuclei
S. Hama, B.C. Clark, E.D. Cooper, H.S. Sherif and R.L. Mercer
Physical Review C75 (1990) 1766

[Hod71] Nuclear reaction and nuclear structure
P.E. Hodgson
Clarendon Press Oxford (1971)

[Jac65] Partial wave analysis of the (p,2p) reaction
Daphne F. Jackson and Tore Berggren
Nuclear Physics 62 (1965) 353

[Jac66] Quasi-free scattering and nuclear structure
Gerhard Jacob and Th. A. J. Maris
Review of Modern Physics 38 (1966) 121

[Jin92] Electron Coulomb effects in quasielastic (e,e'p) reactions
Y. Jin, D.S. Onley and L.E. Wright
Physical Review C45 (1992) 1311

[Kno89] Radiation Detection and Measurement
G.L. Knoll
John Wiley & Sons (1989)

[Kra87] Introductory Nuclear Physics
K.S. Krane
John Wiley & Sons (1987)

[Leo94] Techniques for Nuclear and Particle Physics Experiments
W.R. Leo
Springer Verlag (1994)

[Li94] Measurement of spin observables in (p,2p) quasi-free scattering from very light nuclei
P. Li
Ph.D. thesis (1994)
Indiana University

[Mad87] A preliminary medium-energy nucleon-nucleon phenomenological optical model potential
D.G. Madland
Los Alamos National Laboratory Report LA-UR 87-3382
(1987 unpublished)

[Mah88] Single -particle potential and quasi particle properties of protons in ^{208}Pb
C. Mahaux and R. Sartor
Nuclear Physics A481 (1988) 381

[McD90] Coulomb-distortion effects an spectroscopic strengths from the (e,e'p) reaction
J.P. McDermott
Physical Review Letters 65 (1990) 1991

[Mea69] The loss of protons by nuclear inelastic interactions in various materials
D.F.Measday and C.Richard-Serre
Nuclear Instruments and Methods 76 (1969) 45-54

[Mer70] Quantum Mechanics
E. Merzbacher
John Wiley & Sons (1970)

[Nac99] Overview 1999. Experimental Nuclear Physics at
National Accelerator Centre [online]
Available: http://www.nac.ac.za/nuclearphysics/reaction.html

[Nad81] Elastic scattering of 80-180 MeV protons and the proton-nucleus optical potential
A. Nadasen, P. Schwandt, P.P. Singh, W.W. Jacobs, A.D. Bacher,
P.T. Debevec, M.D. Kaitchuck and J.T. Meek
Physical Review C23 (1981) 1023

[Nev98] A Study of $^{208}Pb(p,2p)^{207}Tl$ Reaction with a Magnetic Spectrometer at an Incident Energy of 200 MeV
R. Neveling
M.Sc. thesis (1998)
University of Stellenbosch

[New96] Single Proton Transfer on ^{55}Mn
R.T. Newman
Ph.D. thesis (1996)
University of Cape Town

[Pil96] The NAC MBD to VME Conversion Guide
J.V. Pilcher
National Accelerator Center (1996) (Unpublished)

[Red70] Off-shell effects in knockout reactions
Edward F. Redish, G.J. Stephenson, Jr. and Gerald M. Lerner
Physics Review C2 (1970) 1665

[Roy70] Étude des réactions $^{208}Pb(d,^{3}He)^{203}Tl$ et $^{204}Pb(d,He)^{203}Tl$ á 80 MeV
D. Royer, M. Arditi, L. Bimbot, H. Doubre, N. Frascaria, J.P. Grarron et M. Riou
Nuclear Physics A158 (1970) 516

[Sch82] Analyzing power of proton-nucleus elastic scattering between 80 and 180 MeV
P. Schwandt, H.O. Meyer, W.W. Jacobs, A.D. Bacher, S.E. Vigdor, M.D. Kaitchuck and T.R. Donoghue
Physical Review C26 (1982) 55

[Udí93] Spectroscopic factors in ^{40}Ca and ^{208}Pb from (e,e'p): Fully relativistic analysis
J.M. Udías, P. Sarriguren, E. Moya de Guerra, E. Garrido and J.A. Caballero
Physical Review C48 (1993) 2731

[Wag90] Occupation Probabilities of Shell-Model Orbitals
G.J. Wagner
Prog. Part. Nucl. Phys. 24, p17 (1990)

[Won90] Introductory Nuclear Physics
S.S.M. Wong
Prentice Hall (1990)

[Yod94] IUCF VME Data Acquisition System User Information
N.R. Yoder
Indiana University Cyclotron Facility (1994) (Unpublished)